DEPARTMENT OF PHYSICS
UNIVERSITY OF JYVÄSKYLÄ
RESEARCH REPORT No. 3/2005

FLUID FLOW IN POROUS MEDIA WITH THE LATTICE-BOLTZMANN METHOD

BY
URPO AALTOSALMI

Academic Dissertation
for the Degree of
Doctor of Philosophy

To be presented, by permission of the
Faculty of Mathematics and Science
of the University of Jyväskylä,
for public examination in Auditorium FYS-1 of the
University of Jyväskylä on July 29, 2005
at 12 o'clock

Jyväskylä, Finland
July, 2005

ISBN 978-951-39-3160-5
URN:ISBN:978-951-39-3160-5

Preface

The work reviewed in this thesis has been carried out during the years 1999-2004 in the Department of Physics at the University of Jyväskylä.

First I would like to thank my supervisors Professor Jussi Timonen, Professor Markku Kataja and Docent Antti Koponen for their invaluable contributions during the preparation of the enclosed articles and this thesis. I also wish to thank Dr. Rudolf Hilfer, Dr. Rune Holmstad, Dr. Christian Manwart, Professor Shri Ramaswamy and Mr. Marko Rasi for collaboration and their contributions to the enclosed articles. For an inspiring working atmosphere and advice with many practical problems, I would like to thank my work-mates in room FL348. The financial support from the International PhD Programme in Pulp and Paper Science and Technology (PaPSaT) and the University of Jyväskylä is gratefully acknowledged.

Finally, I want to thank my parents and friends for their support during this work.

Jyväskylä, July 2005

Urpo Aaltosalmi

Abstract

Aaltosalmi, Urpo
Fluid flow in porous media with the lattice-Boltzmann method
Jyväskylä: University of Jyväskylä, 2005, 158 p.
(Research report/Department of Physics, University of Jyväskylä,
ISSN 0075-465X; 3/2005)
ISBN 951-39-2222-7
Diss.

The lattice-Boltzmann method has recently become a useful approach for computational fluid dynamics. Simple implementation of boundary conditions together with inherent grid generation makes the method geometrically very versatile, and it is thus convenient for simulating complex systems such as fluid flow in porous media. Solving realistic flow problems has become feasible because of increased computing capabilities and parallel processing, for which the spatially local updating rules of the lattice-Boltzmann method are particularly suitable. In this thesis, fluid dynamics in porous media and the basic principles of the lattice-Boltzmann method are first introduced. Application of the method to flow simulations is then discussed in terms of some practical problems, such as boundary conditions, discretization errors and numerical stability, and benchmark studies are carried out to validate the method. Finally, several single-fluid flow problems in irregular 3D geometries are analyzed numerically. The lattice-Boltzmann simulations are used to find out the quality of tomographic imaging techniques and numerical models of porous media. Dependence of permeability on porosity and other structural properties such as specific surface area, tortuosity, and shape and orientation of particles in the medium, are demonstrated and compared to those given by other methods, theory and experiment. The effects of size and resolution of tomographic images of several paper grades are examined by simulating fluid flow through the images and by image analysis. The lattice-Boltzmann, image analysis and experimental results for the permeability of tomographic images of hand sheets with different refining levels are reported. Models and a tomographic image of sandstone are analyzed by comparing the lattice-Boltzmann and finite-difference results also with experiment. The effect of specific surface area, via fines content and shape of fibres, is demonstrated by the lattice-Boltzman flow simulations through fibre-web-model samples.

Keywords lattice-Boltzmann method, fluid dynamics, porous media, permeability.

Author's address Urpo Aaltosalmi
Department of Physics
University of Jyväskylä
Finland

Supervisors Professor Jussi Timonen
Department of Physics
University of Jyväskylä
Finland

Professor Markku Kataja
Department of Physics
University of Jyväskylä
Finland

Docent Antti Koponen
Department of Physics
University of Jyväskylä
Finland

Reviewers Doctor Drona Kandhai
Section of Computational Sciences
University of Amsterdam
Netherlands

Professor Jouni Paltakari
Laboratory of Paper Technology
Helsinki University of Technology
Finland

Opponent Docent Pentti Saarenrinne
Institute of Energy and Process Engineering
Tampere University of Technology
Finland

List of Publications

A.I. U. AALTOSALMI, M. KATAJA, A. KOPONEN, J. TIMONEN, A. GOEL, G. LEE, AND S. RAMASWAMY, *Numerical analysis of fluid flow through fibrous porous materials*, JPPS **30** (9) (2004) 251–255.

A.II. C. MANWART, U. AALTOSALMI, A. KOPONEN, R. HILFER, AND J. TIMONEN, *Lattice-Boltzmann and finite difference simulations for the permeability of three-dimensional porous media*, Phys. Rev. E **66** (2002) 016702.

A.III. S. RAMASWAMY, M. GUPTA, A. GOEL, U. AALTOSALMI, M. KATAJA, A. KOPONEN, AND B. V. RAMARAO, *Efficient simulation of flow and transport in porous media*, Colloids and Surfaces A: Physicochemical and Engineering Aspects **241** (1) (2004) 323–333.

A.IV. R. HOLMSTAD, U. AALTOSALMI, S. RAMASWAMY, M. KATAJA, A. KOPONEN, A. GOEL, AND Ø. W. GREGERSEN, *Comparison of 3D structural characteristics of high and low resolution X-ray microtomographic images of paper*, Submitted for publication in NPPRJ.

A.V. M. RASI, A. KOPONEN, U. AALTOSALMI, J. TIMONEN, M. KATAJA, AND K.J. NISKANEN, *Permeability of paper: Experiments and numerical simulations*, in TAPPI International Paper Physics conference, TAPPI Press, Atlanta, 1999, pp. 297–306.

The author of this thesis has performed all the lattice-Boltzmann simulations involved in the enclosed articles in Appendices A.I–A.V. The author has written the first draft of the article A.I and parts of articles A.II–A.IV, and has participated in writing the lattice-Boltzmann part of article A.V.

Contents

Chapter 1

Introduction

Fluid flow in a porous medium is a common phenomenon in nature, and in many fields of science and engineering. Important everyday flow phenomena include transport of water in living plants and trees, and fertilizers or wastes in soil. Moreover, there is a wide variety of technical processes that involve fluid dynamics in various branches of process industry. The importance of improving our understanding of such processes arises from the high amount of energy consumed by them. In oil recovery, for example, a typical problem is the amount of unrecovered oil left in oil reservoirs by traditional recovery techniques [1]. In many cases the porous structure of the medium and the related fluid flow are very complex, and detailed studies of these flows pose demanding tasks even in the case of stationary single-fluid flow.

In experimental and theoretical work on fluid flow in porous materials it is typically relevant to find correlations between material characteristics, such as porosity and specific surface area, and flow properties. The most important phenomenological law governing the flow properties, first discovered by Darcy [2], defines the permeability as a conductivity to fluid flow of the porous material. Permeability is given by the coefficient of linear response of the fluid to a non-zero pressure gradient in terms of the flux induced [3, 4].

Some of the material properties that affect the permeability, *e.g.* tortuosity, are difficult to determine accurately with experimental techniques, which have been, for a long time, the only practical way to study many fluid-dynamical problems. Improvement of computers and the subsequent development of methods of computational fluid dynamics (CFD) have gradually made it possible to directly solve many complex fluid-dynamical problems. Flow is determined by its velocity and pressure fields, and the CFD methods typically solve these in a discrete computational grid generated in the fluid phases of the system. Traditionally CFD has concentrated on finding solution to differential continuum equations that govern the fluid flow. The results of many conventional methods are sensitive to grid generation which most often can be the main effort in the application. A successfully generated grid is typically an irregular mesh including knotty details that follow the expected stream-

lines [5]. Streamlines are not, however, always *ab initio* easily known. Lattice-based methods with a regular computational grid could be well suited for complex fluid flows found especially in porous media.

The dynamics of fluid flows are generated at the microscopic level and could be, in principle, modelled with direct molecular-dynamics simulations. Obviously, in practice it is unreasonable to solve real macroscopic systems with this approach. Fluid can also be modelled with simplified (more macroscopic) models, just as many other dynamical systems. One of such simplified approaches to CFD is the mesoscopic lattice-Boltzmann method (LBM) [6–11]. It can be considered as a special finite-difference form of the continuum Boltzmann equation [12], but historically it is a pre-averaged improvement to its predecessor, the lattice-gas method [8, 13, 14]. The evolution of lattice-gas methods started after discovering that fluid could indeed be simulated with simple discrete models [15]. In these methods the fluid is modelled by particles that move on a regular lattice which often must be chosen in a special way. The particles propagate to their adjacent lattice points and re-distribute their momenta in the subsequent collisions. Many different lattice-gas and Boltzmann models have been developed for various kinds of two- and three-dimensional lattices, with different connectivities and collision rules [6–8, 16].

The early lattice-gas methods had some deficiencies, and to improve the situation several lattice-Boltzmann models were formulated. The first of them was the so-called nonlinear lattice-Boltzmann model [17] in which a mean-value representation of particles eliminated the problem of statistical noise. In order to overcome the complexity of the lattice-gas collision operator used also in the lattice-Boltzmann models, a linearized enhanced-collision method was developed [18]. Furthermore, Galilean invariant macroscopic behaviour was achieved by including so-called rest particles and by using a Maxwellian velocity distribution for the particles [19]. The simplest and a very widely used lattice-Boltzmann model is the lattice-BGK (Bhatnagar-Gross-Krook) model in which the collision operator is based on the single-relaxation-time approximation to the local equilibrium distribution [6]. Noticeable are also the multiple-relaxation-time (MRT) lattice-Boltzmann models [20] that can be tuned *e.g.* to offer increased numerical stability [21], especially in the high-Reynolds number simulations [22].

When the lattice-gas method, and a bit later, the lattice-Boltzmann method were introduced, they were found to be very useful for simulating fluid flow in porous media. One of the earliest studies, reported in Ref. [23] in 1987, was concerned with the validity of Darcy's law for a 2D system constructed of randomly placed solid points. The results of fluid-flow simulations in a complex 2D medium were reported in a classical paper [24] that appeared in the following year. One of the first 3D studies, that of Ref. [25], demonstrated the validity of the lattice-Boltzmann model for simulations of fluid flow in complex 3D geometries. The validity of the Kozeny law was demostrated in Ref. [26] for an array of randomly placed spheres.

Fluid-flow simulations were performed in a fractal 3D medium in Ref. [27], and in a digital image of Fointainebleau sandstone in Ref. [28]. In addition to flows in porous media the most successful applications of the lattice-Boltzmann method have been multiphase flows [14,28] and suspension flows [29,30].

Realistic computer simulations of fluid flow in porous media necessitate an adequate description of the pore structure, which is modelled or found experimentally [31]. Recently, improved techniques of X-ray microtomography [32] have been used to describe the three-dimensional structure of various porous materials. Combining tomographic imaging with LBM makes realistic flow simulations feasible, and provides effective tools for studying various transport and structural properties of these materials. Realistic simulations of fluid flow in complex geometries can however be very demanding in terms of computational resources, also when lattice-Boltzmann methods are used.

The main objective of this thesis was to get new insight into fluid flow in porous media by using advanced lattice-Boltzmann methods in combination with realistic tomographic or numerical reconstructions of these media. The ambition was to understand in particular the permeability of porous materials and its dependence on other macroscopic material parameters.

We begin by discussing in Chapter 2 the basic concepts and properties of fluid flow, especially in porous media. In Chapter 3 we introduce the lattice-Boltzmann method. We show how the flow equations are obtained from microscopic dynamics of the system and introduce several variations of the lattice-Boltzmann method. We discuss the error sources and present benchmark studies and samples of porous media. In Chapter 4 we present our simulation results for saturated flow through numerical model structures, tomographic images of various paper grades, paper-machine wires and sandstone. We compare the simulation results with those given by theoretical predictions, other numerical methods and experiments. Special attention is given to permeability that is, as a rule, explained with other material and flow properties.

Chapter 2

Fluid flow in porous media

2.1 Concept of fluid

Fluid dynamics (also called fluid mechanics) is the study of moving (deformable) matter, and includes liquids and gases, plasmas and, to some extent, plastic solids. From a 'fluid-mechanical' point of view, matter can, in a broad sense, be considered to consist of fluid and solid, in a one-fluid system the difference between these two states being that a solid can resist shear stress by a static deformation, but a fluid can not [4, 33]. Notice also that thermodynamically a distinction between the gas and liquid states of matter cannot be made if temperature is above that of the so-called critical point, and below that temperature the only essential differences between these two phases are their differing equilibrium densities and compressibilities.

2.1.1 Fluid as a continuum

Gases consist of molecules that have a very large mean distance between them as compared with the molecular size, while in liquids this mean distance is not much bigger than in the solid phase, at most a few times the size of the molecule. Especially in the gas phase molecules move almost freely relative to each other, and in a given control volume the number of molecules changes continuously. Because of this microscopic uncertainty, fluid density has no precise meaning unless the control volume is large in comparison with the intermolecular spacing. However, if the chosen volume is too large, there could be variation in the bulk density of the molecules due to other effects. A reasonable value for such a volume is thus about $10^{-9}\ \mathrm{mm}^3$ for all liquids and for gases at atmospheric pressure [33]. Most practical problems have physical dimensions much larger than this size so that they display fluid properties with practically continuous spatial variation. Such a fluid can be called a continuum, and well-defined derivatives (of needed order) of the relevant variables can be used to describe its dynamics.

The local equilibrium of such a fluid is produced and maintained by collisions

between molecules, which occur in a characteristic time scale τ. In classical fluids, τ is of the order of 10^{-10} to 10^{-14} seconds [34]. The mean free path λ_{mfp} between collisions of the molecules is the related length scale.

In systems with macroscopic motion, the equilibrium states are not homogeneous. Disturbances from the equilibrium states vary in time and length scales set by τ and λ_{mfp}, and the macroscopic variables of the system have slow temporal variations at long wavelengths. For these variables, there is a large amount of equilibrating collisions, and dynamical disturbances are small in space at all times.

In order to determine whether the above conditions for conventional fluid dynamics are satisfied, the Knudsen number should be evaluated for the problem. The Knudsen number Kn is the ratio of the molecular mean free path λ_{mfp} to a representative physical length scale λ_0 of the obstacles and flow channels,

$$Kn = \lambda_{\mathrm{mfp}}/\lambda_0. \tag{2.1}$$

Flow fields cannot be described by conventional fluid dynamics as described in the following sections unless this ratio is small.

2.2 Basic flow relations

The motion of a fluid is described by the basic hydrodynamic equations, the continuity equation

$$\partial_t \rho + \nabla \cdot (\rho \mathbf{u}) = 0, \tag{2.2}$$

which expresses the conservation of mass, and the momentum equation

$$\partial_t (\rho \mathbf{u}) + \nabla \cdot (\rho \mathbf{u}\mathbf{u}) = -\nabla p + \nabla \cdot \tau + \rho \mathbf{g}, \tag{2.3}$$

which expresses the conservation of momentum [33,35]. Here ρ is the fluid density, $\mathbf{u}$ the fluid velocity, p the hydrostatic pressure, τ the fluid stress tensor, and $\mathbf{g}$ the acceleration due to external forces including *e.g.* the effect of gravity on the fluid. The equation for energy conservation can be written as [33]

$$\rho \frac{d\hat{u}}{dt} + p(\nabla \cdot \mathbf{u}) = \nabla \cdot (k \nabla T) + \Phi, \tag{2.4}$$

where T is temperature, k the coefficient of thermal conductivity of the fluid, Φ the viscous dissipation function, and the density of thermal energy $\hat{u} = \hat{u}(p, T)$ is often approximated such that $d\hat{u} \approx c_v dT$, where c_v is the specific heat.

In Newtonian fluids viscous stresses are directly proportional to velocity derivatives, $\tau_{ij} = \partial_i u_j$, and for them Eq. (2.3) reduces to the Navier-Stokes equation [33,35]

$$\partial_t (\rho \mathbf{u}) + \nabla \cdot (\rho \mathbf{u}\mathbf{u}) = -\nabla p + \mu \nabla^2 \mathbf{u} + \rho \mathbf{g}, \tag{2.5}$$

where μ is the dynamic viscosity of the fluid. For incompressible fluids this equation can also be written in the form

$$\partial_t \mathbf{u} + (\mathbf{u} \cdot \nabla)\mathbf{u} = -\frac{1}{\rho}\nabla p + \nu \nabla^2 \mathbf{u} + \mathbf{g}, \tag{2.6}$$

where $\nu = \mu/\rho$ is the kinematic viscosity of the fluid. Continuity and momentum equations are usually independent of T and they can be solved separately from the energy equation. Equation (2.5) comprises three second-order nonlinear partial differential equations for four unknown variables, i.e. pressure and the three components of velocity, to be solved in space and time. The system is closed by combining it with Eq. (2.2) and using appropriate boundary conditions, such as known pressure or velocity at the inlet and outlet, or at free surfaces. At solid-fluid interfaces the so-called no-slip boundary condition is characteristic of all viscous fluid flows [33]. This means that at a solid wall the fluid velocity is zero with respect to the wall.

Sometimes the fluid-flow equations above can be simplified. The simplest assumption is frictionless flow, for which Eq. (2.5) reduces to the Euler equation

$$\mathbf{g} - \frac{1}{\rho}\nabla p = \partial_t \mathbf{u} + (\mathbf{u} \cdot \nabla)\mathbf{u}. \tag{2.7}$$

Integrating Eq. (2.7) along a streamline in a gravitational field $\mathbf{g} = g\hat{\mathbf{e}}_\mathbf{z}$ produces a relation between pressure, velocity, and elevation of the flow, the Bernoulli equation, which for incompressible steady flow is reduced to

$$p + \frac{1}{2}\rho u^2 + \rho g z = C, \tag{2.8}$$

where C is a constant for each streamline, g the gravitational acceleration and z the elevation. The Bernoulli equation is closely related to the steady-flow energy equation and is widely used, but has many restrictions. For example, on the streamline no shaft work or heat transfer is accepted [33].

In the case of stationary flow with very low inertial forces, the left-hand side of Eq. (2.5) is negligible, and it is reduced to the Stokes equation

$$\nabla p - \rho \mathbf{g} = \mu \nabla^2 \mathbf{u}. \tag{2.9}$$

This relation has great value in theoretical and experimental work related to *e.g.* fluid flows in porous media, where fluid velocities are low. In the flow systems described by the Stokes equation, the pressure drop is directly proportional to the fluid velocity, and only one experiment or simulation is needed to cover this linear range. As a consequence the flow is symmetric: if the force is reversed, the streamlines remain unchanged. In the Stokes flow the fluid motion is also smooth and regular, *i.e.* the flow is laminar. When inertial forces become comparable to viscous forces, *e.g.*

by increasing the flow velocity, the flow begins to have instabilities and enters the 'transition' regime. Still increasing the flow velocity finally turns the flow turbulent, in which case it is dominated by inertial forces that produce eddies, vortices and other dynamical fluctuations.

The ratio of inertial and viscous forces is thus a primary parameter for the behaviour of all Newtonian fluids, and this ratio is the dimensionless Reynolds number [33]

$$Re = \frac{\rho V L}{\mu} = \frac{V L}{\nu}, \tag{2.10}$$

where V and L are the characteristic velocity and length scales of the flow, respectively. Reynolds number provides a criterion for dynamic similarity. If two geometrically similar flow systems of possibly different sizes, fluids or flow rates have the same Reynolds number, they will have a similar flow pattern. There are also many other dimensionless numbers that are very important when simulation results or model experiments are applied to real systems.

In many cases it is advantageous to express the relevant quantities and equations in dimensionless form. For example, the dimensionless form of the Navier-Stokes equation Eq. (2.5) is [35]

$$\partial_{t^*}\mathbf{u}^* + (\mathbf{u}^* \cdot \nabla^*)\mathbf{u}^* = -\nabla^* p^* + \frac{1}{\mathrm{Re}}\nabla^{*2}\mathbf{u}^*. \tag{2.11}$$

2.3 Permeability

2.3.1 Darcy's law

At low Reynolds numbers, the most important relation describing fluid transport through porous media is Darcy's law [3],

$$\mathbf{q} = -\frac{k}{\mu}\nabla p, \tag{2.12}$$

where $\mathbf{q}$ is the volumetric fluid flow through the (homogeneous) medium and k is the permeability coefficient that measures the conductivity to fluid flow of the porous material.

Darcy's law was introduced originally as an empirical relationship based on experiments on steady flow in a vertical homogeneous sand filter [2], and Eq. (2.12) has been found to work very well with a wide variety of natural porous media from sand to granite rocks [1, 3, 4]. Darcy's law may be presented also as a particular, simplified form of the averaged Stokes equation, Eq. (2.9), within its assumptions. The importance of Eq. (2.12) is thus obvious as it governs a Stokesian flow though a porous material and the permeability coefficient k contains all the material dependencies.

When components of volumetric fluid flow exist perpendicular to the applied pressure gradient, then permeability can be expressed as a tensor in Darcy's law Eq. (2.12), while $\mathbf{q}$ is a row vector and ∇p a column vector. For given three principal directions of the pressure gradient, the diagonal elements of the permeability tensor give the fluid conductivity in these three directions and the other elements indicate the conductivity in cross directions.

Many attempts have been made to analytically derive Darcy's law, or more generally, the equations of motion in porous media. In most cases, model media have been employed including *e.g.* the capillary-tube model [3,4,36]. By solving the Navier-Stokes or Stokes equation in these models, one obtains equations of motion and permeability. They involve material properties in terms of *ab initio* unknown coefficients. It is thus understandable that functional correlations between the permeability and other macroscopic properties of the medium are attempted to find also experimentally. Among the most important of such material properties are porosity ϕ and specific surface area S_0, i.e. the pore surface area in a unit volume of the solid material. In practice, for real fluids and materials, these can sometimes be ambiguous. The pore volume of the material can include non-percolating pores, and also some other non-conducting parts, reducing the geometrical porosity to effective porosity [37]. Usually, the difference between these two porosities becomes more pronounced near the percolation threshold, defined as a point where the medium becomes completely blocked. Yet another useful characteristics of porous media is tortuosity τ, which is a measure of the complexity of the flow paths, and a possible definition for it is the ratio of the average length of the flow paths to the thickness of the sample (see Section 2.3.3).

2.3.2 Expressions for permeability

The most widely used expressions, the Kozeny law and the Kozeny–Carman law, that relate permeability to the structural characteristics of the medium have been derived analytically for capillary tube models [3, 4, 38]. The Kozeny law expresses the permeability of the medium in the form

$$k = \frac{\phi^3}{c\tau^2 S^2}, \tag{2.13}$$

where S is the pore surface area in unit volume and c is the so called Kozeny constant that depends on the geometry of the porous sample. For simple capillary-tube models, *e.g.* for cylindrical capillaries, $c = 2$. Tortuosity τ is sometimes embedded into the Kozeny constant, in which case the Kozeny law becomes

$$k = \frac{\phi^3}{cS^2}. \tag{2.14}$$

In terms of the specific surface area $S_0 = S/(1-\phi)$, Eq. (2.14) can be written in the form of the Kozeny–Carman law,

$$k = \frac{1}{cS_0^2}\frac{\phi^3}{(1-\phi)^2}. \tag{2.15}$$

Equations (2.13) – (2.15) can be used to predict the qualitative permeable behaviour of many porous media, but the accuracy of these relations is generally not very good over an extended interval in ϕ. A number of similar formulae, derived especially for fibrous porous materials, can be found in the literature [39]. An example of such a formula, derived by Happel for an array of parallel cylindrical rods perpendicular to the flow, is given by [40]

$$k = \frac{a^2}{8\varphi}(-\ln\varphi + \frac{\varphi^2-1}{\varphi^2+1}). \tag{2.16}$$

Here a is the average radius of the rods and $\varphi = 1-\phi$ the solid-volume fraction.

2.3.3 Tortuosity

The path of the fluid that flows in a porous medium can be microscopically very tortuous and complicated. This phenomenon is present not only in the case of fluid flow but also in the case *e.g.* of electric currents. Tortuosity has been defined in various ways. In the case of capillary models, in Eq. (2.13), tortuosity is introduced as the relation $\tau = 1/\cos\theta$, where θ is the (fixed) angle formed by the capillaries with the normal of the surface of the material (the azimuthal angles of the capillaries are randomly distributed). In terms of the tube length L_e and the thickness of the medium L, tortuosity is thus $\tau = L_e/L$. Some authors prefer however to define the tortuosity as $\tau = (L_e/L)^2$, or as inverses of these two definitions [4, 41].

In general, the flow tortuosity is defined as the ratio of the mean length of flow paths to the thickness of the sample (the direction of mean flow). As shown in Ref. [42], a numerical estimate of tortuosity can be conveniently determined from

$$\tau \equiv \frac{\langle|\mathbf{v}|\rangle}{\langle v_x\rangle}, \tag{2.17}$$

where $|\mathbf{v}|$ is the absolute value of local flow velocity, v_x is the x component of velocity in the direction of mean flow, and $\langle\ \rangle$ denotes spatial average over the pore space. Notice that tortuosity for an arbitrary porous medium is very difficult to measure experimentally. Lately, in addition to the flow tortuosity determined above, also other quantities have been introduced, such as *e.g.* diffusive tortuosity [43] based on random-walk simulations for path lengths in the pore space under consideration. Tortuosity can also be defined without reference to a specific transport mechanism, for example by considering the shortest continuous paths between any two points

within the pore space [44]. Within such a definition tortuosity is just a geometric parameter characteristic of the pore space. In the context of transport phenomena, it is however natural to use a definition like that of Eq. (2.17).

2.3.4 Experiments

Theoretical methods typically rely on analytical models based on simplified pore geometries, in which the structural complexity is often taken into account only statistically [1,4]. In order to make the models mathematically reasonable, many simplifications in the flow dynamics or pore structure are necessary, which usually weakens the ability of the models to describe real systems. Due to these simplifications, theoretical expressions typically include parameters that can be determined by experiments, or lately also by numerical simulations.

The experimental methods used to analyze fluid transport through porous substances vary from quite straightforward measurements [39,45,46] to more complicated approaches, which utilize *e.g.* mercury porosimetry [47], electrical conductivity [48], nuclear magnetic resonance [49], or acoustic properties of the medium [50]. In many practical problems fluid flow is Stokesian, and permeability is always an important quantity. In principle, a permeability experiment with a given fluid comprises the determination of the averaged fluid flux for a given pressure gradient in the Stokes-flow regime. However, these experiments typically suffer from many uncertainties, and the permeabilities measured in this way often depend noticeably on minute experimental details. Also, time consumption may be a problem as, for example, in water-flow experiments through low-porosity rock samples. In addition to the permeability itself, many material characteristics on which the measured permeability depends, can be difficult to determine accurately.

In paper, for example, fibres are hollow and contain fibrils, and the solid phase also includes varying amounts of fines and fillers. The macroscopic porosity that takes part in fluid transport is thus difficult to determine. Wood fibres have also microscopic porosity, which can change the transport properties of paper indirectly as water is absorbed in the fibres and causes their swelling. Moreover, under pressure the structure of paper changes and thereby also its permeability. These structural features of paper may also mean that its permeability could depend on the fluid used in the measurements, in particular gas permeability can be higher than water permeability [51].

One experimental technique applied to transverse and in-plane flow in polymeric fabrics is a Liquid/Air Displacement Analyzer [52], originally developed by TRI/Princeton. In particular, the technique can be used to determine the in-plane water-flow characteristics of paper samples. In this case both paper surfaces are covered with an impermeable plastic tape to prevent liquid from penetrating through the surface, and a hole is punched in the cover tape to apply a pressure difference. The sample can be *e.g.* circular or rectangular, in which case three edges are typically

sealed with glue. The sample is then mounted on a fixture and placed under water. Different vacuum levels are applied through the hole, and the volumetric rate of penetration of water, at a given applied pressure difference, is measured as a function of time by measuring the weight loss of the whole system. From the volumetric rate of penetration, the relative permeability is determined. Due to the heterogeneous nature of paperboard, liquid front propagation during a test may appear uneven [I, 53], but in general the flow follows the form of Darcy's law over a wide range of driving pressures [I, 52].

Chapter 3

Lattice-Boltzmann hydrodynamics

The lattice-Boltzmann method [6–11] is a mesoscopic approach to computational fluid dynamics in which the basic idea is to solve a discretized Boltzmann equation. The macroscopic dynamics of the system can be shown to obey the Navier-Stokes equation. In this method the fluid is modelled by particle distributions that move on a lattice divided to solid and fluid points. During one lattice time step, particles propagate to their adjacent lattice points and redistribute their momenta in the subsequent collisions. Each time step involves also the action *e.g.* of the external forces on the fluid and the boundary conditions at the solid-fluid interfaces.

3.1 From microdynamics to macroscopic hydrodynamics

We denote by $f_i(\mathbf{r}, t)$ the particle density entering at site $\mathbf{r}$ at time t with a velocity pointing in direction $\mathbf{c}_i$, where i labels the lattice directions. For a lattice time step η and lattice spacing λ, the possible particle velocities are

$$\mathbf{v}_i = \frac{\lambda}{\eta}\mathbf{c}_i. \tag{3.1}$$

The evolution equation for f_i is

$$f_i(\mathbf{r} + \lambda\mathbf{c}_i, t + \eta) = f_i(\mathbf{r}, t) + \Omega_i(\mathbf{r}, t), \tag{3.2}$$

where $\Omega_i(\mathbf{r}, t)$ is a model-dependent collision term that decreases or increases the density of type i particles.

In analogy with the kinetic theory of gases, hydrodynamic quantities like density ρ, velocity $\mathbf{u}$ and momentum tensor Π, are obtained from the velocity moments

of distribution f_i [29,54],

$$\rho(\mathbf{r},t) = \sum_{i=1}^{I} f_i(\mathbf{r},t), \tag{3.3}$$

$$\rho(\mathbf{r},t)\mathbf{u}(\mathbf{r},t) = \sum_{i=1}^{I} \mathbf{v}_i f_i(\mathbf{r},t) \tag{3.4}$$

and

$$\Pi_{\alpha\beta}(\mathbf{r},t) = \sum_{i=1}^{I} v_{i\alpha} v_{i\beta} f_i(\mathbf{r},t). \tag{3.5}$$

Here greek letters α and β label the spatial components of the velocity vectors and I is the number of possible directions $\mathbf{c}_i$.

In its simplest form, lattice-Boltzmann dynamics is governed by the collision operator of the lattice-BGK model, $\Omega_i = \frac{1}{\xi}(f_i^{(0)}(\mathbf{r},t) - f_i(\mathbf{r},t))$, based on a single-collision relaxation to the local equilibrium distribution [6]. The evolution equation for a lattice-BGK system is thus

$$f_i(\mathbf{r} + \lambda\mathbf{c}_i, t + \eta) = f_i(\mathbf{r},t) + \frac{1}{\xi}(f_i^{(0)}(\mathbf{r},t) - f_i(\mathbf{r},t)), \tag{3.6}$$

where $f_i(\mathbf{r},t)$ is the particle density on link i at $(\mathbf{r},t)$, ξ is a relaxation parameter, and $f_i^{(0)}$ is the equilibrium distribution which can be chosen to produce the required behaviour of the fluid. This involves not only the mass and momentum conservation, but also many other properties can be obtained with a suitable choice of $f_i^{(0)}$.

A solution to Eq. (3.6) is found by using the Chapman-Enskog expansion, which is commonly used in statistical mechanics for deriving macroscopic laws for relevant physical quantities when the Boltzmann equation is known [9]. Equation (3.6) is discrete in space and time, and it is necessary to assume that the lattice spacing λ and timestep η are small compared to the characteristic length and time scales in the system, L and T. Under these conditions f_i are smoothly varying functions in time and space, and Eq. (3.6) can be expanded around $\mathbf{r}$ and t. Retaining the terms up to second order, we find that

$$\begin{aligned} \eta\partial_t f_i + \lambda(\mathbf{c}_i\cdot\nabla)f_i &+ \frac{\eta^2}{2}\partial_t^2 f_i + \frac{\lambda^2}{2}(\mathbf{c}_i\cdot\nabla)^2 f_i \\ +\lambda\eta(\mathbf{c}_i\cdot\nabla)\partial_t f_i &= \Omega_i, \end{aligned} \tag{3.7}$$

where Ω_i is the collision operator defined above. In the Chapman-Enskog method a perturbation expansion for f_i is introduced,

$$f_i = f_i^{(0)} + \epsilon f_i^{(1)} + \epsilon^2 f_i^{(2)} + \ldots, \tag{3.8}$$

where ϵ is a small parameter. In order to determine the $f_i^{(l)}, l = 0, 1, \ldots$, uniquely

and consistently, it is necessary to assume that the macroscopic quantities ρ and $\rho\mathbf{u}$ are entirely given by the zeroth order terms of the expansion [9]. We thus find

$$\rho = \sum_{i=1}^{I} f_i^{(0)} \quad \text{and} \quad \rho\mathbf{u} = \sum_{i=1}^{I} \mathbf{v}_i f_i^{(0)}, \tag{3.9}$$

and moreover

$$\sum_{i=1}^{I} f_i^{(l)} = 0, \quad \sum_{i=1}^{I} \mathbf{v}_i f_i^{(l)} = 0, \quad \text{for} \quad l \geq 1. \tag{3.10}$$

With respect to λ and η, different phenomena are related to different forms of scaling factors. For instance, fluid convection is related to a coefficient of the order η/λ, and dissipative forces to one of the order λ^2/η [9, 13]. Therefore, no single scaling form comprising λ and η exists, and it is appropriate to consider two macroscopic time scales, T_1 and T_2, satisfying

$$\frac{\eta}{T_1} = \mathrm{O}(\epsilon), \quad \frac{\eta}{T_2} = \mathrm{O}(\epsilon^2), \tag{3.11}$$

and one macroscopic length scale L_1 satisfying

$$\frac{\lambda}{L_1} = \mathrm{O}(\epsilon). \tag{3.12}$$

Two time variables t_1 and t_2 are thus defined such that

$$t = \frac{t_1}{\epsilon} + \frac{t_2}{\epsilon^2}, \tag{3.13}$$

and also a macroscopic space variable $\mathbf{r}_1$ such that $\mathbf{r} = \mathbf{r}_1/\epsilon$. The differentials ∂_t and ∂_α become

$$\partial_t = \epsilon\partial_{t_1} + \epsilon^2\partial_{t_2} \tag{3.14}$$

and

$$\partial_\alpha = \epsilon\partial_{1\alpha}. \tag{3.15}$$

With these time and space derivatives, we can now identify the various orders of ϵ that appear on the left-hand side of Eq. (3.7), whereas the right-hand side, $\Omega_i = \frac{1}{\xi}(f_i^{(0)} - f_i)$, still needs to be expressed in terms of the equilibrium distribution $f_i^{(0)}$.

3.2 A two-dimensional model

For solution of Eq. (3.6) by the Chapman-Enskog expansion Eq. (3.8), we need to specify the lattice and the equilibrium distribution $f_i^{(0)}$, for which there are several constraints to fulfill. A fluid-flow model has to be independent of the choice of the

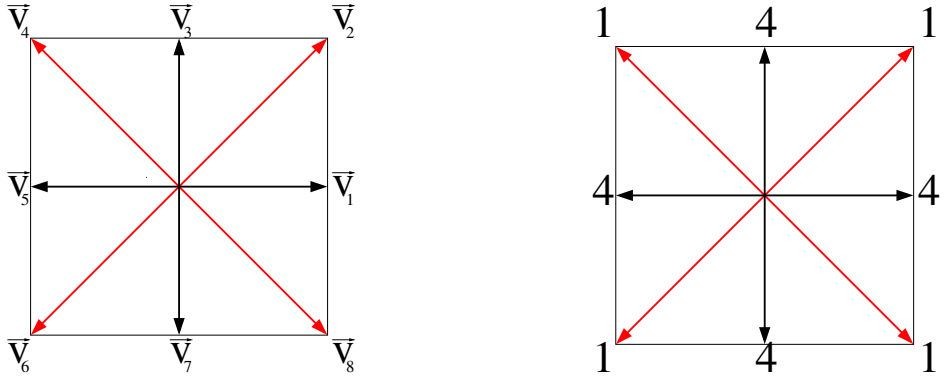

FIGURE 3.1 Left: In the D2Q8 model the particles at each lattice point can propagate to their eight neighbours with two different speeds. Right: The masses associated with the fluid particles propagating in different directions.

coordinate system, *i.e.* isotropic. Furthermore, within the lattice-Boltzmann method, in addition to mass and momentum conservation, we must require Galilean invariance [9].

Here we concider for simplicity the lattice-BGK D2Q8 model (D2 denotes the dimensions of the lattice (2), and Q8 denotes the number of links per lattice point (8) [6]). In the D2Q8 model, each lattice point is connected to its nearest and next-nearest neighbours. Thus there are eight different direction for the particles to propagate with two different particle speeds v_i: $1 \cdot \frac{\lambda}{\eta}$ and $\sqrt{2} \cdot \frac{\lambda}{\eta}$. All velocities do not have the same weight (mass) m_i, and an isotropic model is obtained with the choice $m_i = 4$ for the links to the nearest neighbours (odd i), and $m_i = 1$ for the links to the next-nearest neighbours (even i) as shown in Fig. 3.1 [9]. With this choice the following properties [9] are fulfilled:

$$\sum_{i=1}^{8} m_i c_{i\alpha} = 0, \tag{3.16}$$

$$\sum_{i=1}^{8} m_i c_{i\alpha} c_{i\beta} = 12 v^2 \delta_{\alpha\beta}, \tag{3.17}$$

$$\sum_{i=1}^{8} m_i c_{i\alpha} c_{i\beta} c_{i\gamma} = 0, \tag{3.18}$$

$$\sum_{i=1}^{8} m_i c_{i\alpha} c_{i\beta} c_{i\gamma} c_{i\delta} = 4 v^4 (\delta_{\alpha\beta}\delta_{\gamma\delta} + \delta_{\alpha\gamma}\delta_{\beta\delta} + \delta_{\alpha\delta}\delta_{\beta\gamma}), \tag{3.19}$$

where $v = \lambda/\eta$ is the modulus of $\vec{v}_i$ for odd i.

3.2.1 Local equilibrium

A natural choice for the equilibrium distribution $f_i^{(0)}$ as a function of quantities ρ and $\rho\mathbf{u}$ is now [9]

$$\begin{aligned} f_i^{(0)} &= m_i F_i^{(0)} \\ &\equiv m_i \left(a\rho + \frac{b}{v^2}\rho \mathbf{v}_i \cdot \mathbf{u} + \rho e \frac{u^2}{v^2} + \rho \frac{h}{v^4} (\mathbf{v}_i \cdot \mathbf{u})^2 \right). \end{aligned} \tag{3.20}$$

Here a, b, e and h are constants to be determined so that the required properties of the fluid are obtained. The collision operator Ω_i must conserve mass and momentum, *i.e.*

$$\sum_{i=1}^{8} \Omega_i = 0, \quad \sum_{i=1}^{8} \mathbf{v}_i \Omega_i = 0, \tag{3.21}$$

which actually implies Eqs. (3.9). Using in addition the fact that $\sum_{i=1}^{8} m_i = 20$, and Eqs. (3.16) and (3.17), we obtain [9]

$$a = \frac{1}{20}, \quad b = \frac{1}{12}, \quad 12h + 20e = 0. \tag{3.22}$$

Moreover, in zeroth order we find [9] for the momentum tensor Eq. (3.5),

$$\Pi_{\alpha\beta}^{(0)} = \sum_{i=1}^{8} m_i v_{i\alpha} v_{i\beta} F_i^{(0)} \tag{3.23}$$

$$= 12v^2 \left(a + (e + \frac{h}{3}) \frac{u^2}{v^2} \right) \rho \delta_{\alpha\beta} + 8h\rho u_\alpha u_\beta. \tag{3.24}$$

In order to satisfy Galilean invariance, we choose

$$h = \frac{1}{8}, \tag{3.25}$$

which implies

$$e = -\frac{3}{40}. \tag{3.26}$$

The expression for $\Pi_{\alpha\beta}^{(0)}$ now reads

$$\Pi_{\alpha\beta}^{(0)} = p\delta_{\alpha\beta} + \rho u_\alpha u_\beta, \tag{3.27}$$

where the hydrostatic pressure p is given by

$$p = 12v^2 \left(a + (e + \frac{h}{3}) \frac{u^2}{v^2} \right) \rho = \frac{3}{5} v^2 \left(1 - \frac{2}{3} \frac{u^2}{v^2} \right) \rho. \tag{3.28}$$

We can now write

$$\Pi^{(0)}_{\alpha\beta} = c_s^2 \rho \delta_{\alpha\beta} + \mathrm{O}(u^2), \tag{3.29}$$

where the speed of sound c_s is

$$c_s^2 = \frac{3}{5} v^2. \tag{3.30}$$

In Eq. (3.28), pressure is velocity dependent, which is an unphysical artifact. To remove this contribution, rest particles are included in the lattice-BGK D2Q9 model [55] (see Eq. (3.44) in Sec. 3.3). The velocity of the rest particles is zero, and they do not propagate to adjacent lattice sites, but take part in the collisions.

3.2.2 Navier-Stokes equation

The derivation of the Navier-Stokes equation begins with expanding the Boltzmann equation Eq. (3.6), and involves the use of Eqs. (3.11), (3.12) and (3.21). After some algebra one obtains [9]

$$\partial_t \rho u_\alpha + \partial_\beta \left[\Pi_{\alpha\beta} + \frac{\eta}{2} (\epsilon \partial_{t_1} \Pi^{(0)}_{\alpha\beta} + \partial_\gamma S^{(0)}_{\alpha\beta\gamma}) \right] = 0, \tag{3.31}$$

where $\partial_t = \epsilon \partial_{t_1} + \epsilon^2 \partial_{t_2}$ and $\partial_\alpha = \epsilon \partial_{1\alpha}$ (Eqs. (3.14) and (3.15)) take into account the different time scales of the problem. Above, $S^{(0)}_{\alpha\beta\gamma}$ is defined as

$$S^{(0)}_{\alpha\beta\gamma} = \sum_{i=1}^{8} m_i v_{i\alpha} v_{i\beta} v_{i\gamma} F_i^{(0)}. \tag{3.32}$$

Derivation of $S^{(0)}_{\alpha\beta\gamma}$, and the momentum tensor $\Pi_{\alpha\beta}$, is now needed. $\Pi^{(0)}_{\alpha\beta}$ in the momentum tensor $\Pi_{\alpha\beta} = \Pi^{(0)}_{\alpha\beta} + \Pi^{(1)}_{\alpha\beta} + \dots$ was obtained in the previous section, but now also the first-order term $\Pi^{(1)}_{\alpha\beta}$ is needed. The first-order correction to the velocity distribution F_i can be derived by solving Eq. (3.7) using Eqs. (3.8), (3.14) and (3.15) in terms of ϵ. We find that

$$\Omega_i(F) = \Omega_i(F^{(0)}) + \epsilon \sum_{j=1}^{6} \left(\frac{\partial \Omega_i(F^{(0)})}{\partial F_j} \right) F_j^{(1)} + \mathrm{O}(\epsilon^2). \tag{3.33}$$

The collision operator must be at least of order ϵ^1 [9], but the right-hand side of Eq. (3.33) has a contribution of order $\mathrm{O}(\epsilon^0)$, which means that $\Omega(F^{(0)}) = 0$. A vanishing collision term is in accordance with the fact that the equilibrium solutions $F_i^{(0)}$ are local, corresponding to a situation where the rate of each type of collision equilibrates. The first-order equation is obtained from Eqs. (3.7) and (3.33) [9]:

$$\partial_{t_1} F_i^{(0)} + \partial_{1\alpha} v_{i\alpha} F_i^{(0)} = \frac{1}{\eta} \sum_{j=1}^{6} \left(\frac{\partial \Omega_i(F^{(0)})}{\partial F_j} \right) F_j^{(1)}. \tag{3.34}$$

Once the equilibrium solutions $F_i^{(0)}$ are known, the first order terms $F_i^{(1)}$ are obtained from Eq. (3.34). After some calculations we find [9]

$$F_i^{(1)} = -\eta\xi\frac{b}{v^2}(v_{i\alpha}v_{i\beta} - \frac{av^2}{b}\delta_{\alpha\beta})\partial_{1\alpha}\rho u_\beta. \tag{3.35}$$

$F_i^{(1)}$ can be substituted into the first order term $\Pi_{\alpha\beta}^{(1)}$ of the momentum tensor using $\epsilon\partial_{1\gamma} = \partial_\gamma$ [9]:

$$\begin{aligned}\epsilon\Pi_{\alpha\beta}^{(1)} &= \epsilon\sum_{i=1}^{8} m_i v_{i\alpha}v_{i\beta}F_i^{(1)} &(3.36)\\ &= \eta v^2\xi[(12a-4b)\delta_{\alpha\beta}\nabla\cdot(\rho\mathbf{u}) \\ &\quad -4b(\partial_\beta\rho u_\alpha + \partial_\alpha\rho u_\beta)]. &(3.37)\end{aligned}$$

By using the $F_i^{(0)}$ of Eq. (3.20), we can express $S_{\alpha\beta\gamma}^{(0)}$ in the form [9]

$$\begin{aligned}S_{\alpha\beta\gamma}^{(0)} &= \sum_{i=1}^{8} m_i v_\alpha v_\beta v_\gamma F_i^{(0)} &(3.38)\\ &= \frac{v^2}{3}\rho(u_\gamma\delta_{\alpha\beta} + u_\beta\delta_{\alpha\gamma} + u_\alpha\delta_{\beta\gamma}). &(3.39)\end{aligned}$$

Now, Eqs. (3.27), (3.37) and (3.39) can be substituted into Eq. (3.31) and, after some algebra, we find [9] that

$$\begin{aligned}&\partial_t\rho u_\alpha + \rho u_\beta\partial_\beta u_\alpha + u_\alpha\nabla\cdot(\rho\mathbf{u}) = \\ &-\partial_\alpha p + \eta v^2\left(\frac{\xi}{3} - \frac{1}{6}\right)\nabla^2\rho u_\alpha + \\ &\eta v^2\left[\xi(\frac{2}{3} - 12a) - (\frac{1}{3} - 6a)\right]\partial_\alpha\nabla\cdot\rho\mathbf{u}.\end{aligned} \tag{3.40}$$

In the case of incompressible fluid, $\nabla\cdot(\rho\mathbf{u}) = 0$, we now find the usual Navier-Stokes equation,

$$\partial_t\mathbf{u} + (\mathbf{u}\cdot\nabla)\mathbf{u} = -\frac{1}{\rho}\nabla p + \nu_{lb}\nabla^2\mathbf{u}, \tag{3.41}$$

where

$$\nu_{lb} = \eta v^2\frac{2\xi - 1}{6} \tag{3.42}$$

is the kinematic viscosity of the lattice-Boltzmann fluid. According to Eq. (3.42) the kinematic viscosity ν is independent of fluid density. In addition ξ is a free parameter which can be used to adjust the viscosity within some range. We get arbitrarily small viscosities when $\xi \to \frac{1}{2}$, but in practice viscosity must not be too small, as the dissipation length scale should always be much bigger than the lattice spacing λ [9].

The lattice-Boltzmann algorithm may become unstable with very small values of ξ. From Eq. (3.6) it is evident that relaxation of f_i towards $f_i^{(0)}$ depends on ξ [6]. For $\xi > 1$ relaxation is called subrelaxation, as f_i relaxes monotoneously towards $f_i^{(0)}$. For $\xi = 1$, the velocity distribution is immediately relaxed, and for $1/2 < \xi < 1$, relaxation is called over-relaxation, and f_i fluctuates around $f_i^{(0)}$ with exponentially diminishing amplitude of fluctuation. The values $\xi \leq 1/2$ cannot be used since the algorithm would diverge or a negative viscosity would be implied.

3.3 Other lattice-Boltzmann models

Various different formulations of lattice-Boltzmann models can be found in the literature. In the simplest of them, the lattice-BGK models, the differences are in *e.g.* the connectivity of the lattice, the use of rest particles, and the realizations of the equilibrium distributions or the collision operator. In two dimensions the most common model is the D2Q9 model, which is the D2Q8 model with the rest particles included. A hexagonal lattice with six moving populations and one rest-particle population leads to the D2Q7 model [19].

The lattice-Boltzmann method was originally developed from the lattice-gas method, for which there is no three-dimensional lattice that would yield isotropy. Hence a 3D projection of a 4D face-centered hyper-cubic (fchc) lattice [8] is regularly used, and this D3Q19 lattice was also the first lattice used in 3D lattice-Boltzmann simulations [7]. In this model each lattice point is connected to its six nearest and twelve next-nearest neighbours in a cubic lattice (see Fig. 3.2). The D3Q15 model [6] was developed as a result of relative freedom in choosing the lattice-Boltzmann equilibrium distribution, and the subsequent freedom in choosing the structure of the simulation lattice. In the D3Q15 model each lattice point is connected to its six nearest and eight second-next-nearest neighbours (see Fig. 3.2). In both these 3D models rest particles are included, which improves the accuracy of the models, removes the unphysical velocity dependence of pressure [56], and stabilizes the system for small relaxation times ξ [57]. By excluding the rest particles from the D3Q15 and D3Q19 models, the D3Q14 and D3Q18 models are obtained, respectively. In the D3Q13 model [16] each lattice point is connected to its twelve next-nearest neighbours and rest particles are included.

In addition to Eq. (3.20), the lattice-Boltzmann equilibrium distribution of these models can be chosen in many other ways [6, 30, 58, 59]. A common choice is [6]

$$f_i^{(0)} = m_i \rho \left(1 + \frac{1}{c_s^2}(\mathbf{c}_i \cdot \mathbf{v}) + \frac{1}{2c_s^4}(\mathbf{c}_i \cdot \mathbf{v})^2 - \frac{1}{2c_s^2} v^2 \right), \tag{3.43}$$

where the m_i are the weight factors that depend on the model and the length of the link vectors $\mathbf{c}_i$, and $c_s = 1/\sqrt{3}$ is the speed of sound. For the D2Q9 model, the weights m_i are $\frac{4}{9}$, $\frac{1}{9}$ and $\frac{1}{36}$ for the rest particle and the particles moving to the

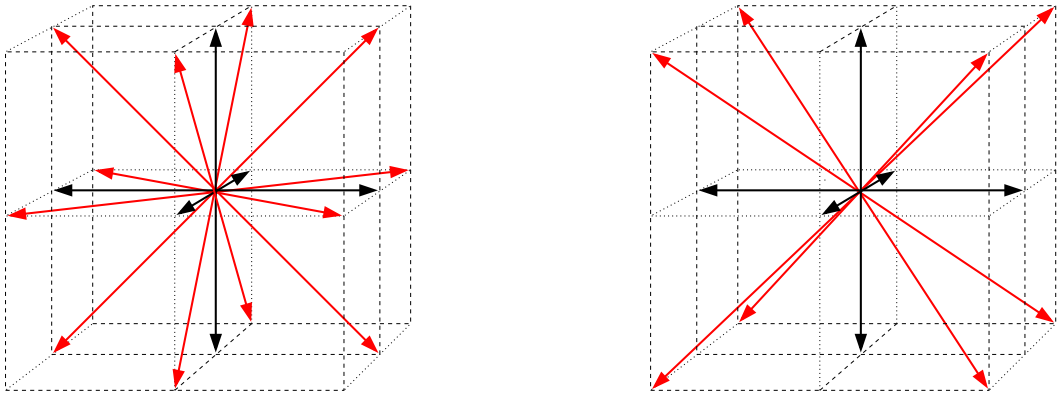

FIGURE 3.2 Lattice structures of the D3Q19 (left) and D3Q15 (right) models.

nearest and next-nearest neighbour sites, respectively. The corresponding numbers for the D3Q19 model are $\frac{1}{3}$, $\frac{1}{18}$ and $\frac{1}{36}$. For the D3Q15 model, the weights m_i are $\frac{2}{9}$, $\frac{1}{9}$ and $\frac{1}{72}$ for the rest particle and the particles moving to the nearest and second-next-nearest neighbour sites, respectively. In these models, the kinematic viscosity is $\nu = (2\xi - 1)/6$ [6], and the fluid pressure is

$$p(\mathbf{r}, t) = c_s^2(\rho(\mathbf{r}, t) - \bar{\rho}) \equiv c_s^2 \Delta\rho, \tag{3.44}$$

where $\bar{\rho}$ is the mean density of the fluid.

The assumption that $\xi = 1$ simplifies the evaluation of the lattice-Boltzmann equations so that models with only four real numbers, namely the density and the three components of velocity [60], are needed in this case.

3.3.1 The multiple-relaxation-time lattice-Boltzmann model

Because of its simplicity, the lattice-BGK equation model has become the most popular lattice-Boltzmann model in spite of its deficiences. The multiple-relaxation-time (MRT) lattice-Boltzmann equation overcomes some problems of the LBGK model, such as a fixed Prandtl number Pr$\equiv \nu/\kappa$, where κ is the thermal diffusivity (Pr $= 1$ for the BGK model), and a fixed ratio of the kinematic to the bulk viscosity. Successfull applications of the MRT lattice-Boltzmann model include formulation of optimal boundary conditions [29,61], interface conditions for multi-phase flows [62] and free surfaces [63,64], thermal and viscoelastic models [65], and models with reduced lattice symmetries [16, 66].

Instead of the single-collision equilibration of the LBGK model the MRT model has a collision matrix S and multiple relaxation times, and its evolution equation is given by [22]

$$|f_i(\mathbf{r} + \lambda\mathbf{c}_i, t + \eta)\rangle - |f_i(\mathbf{r}, t)\rangle = -S(|f_i(\mathbf{r}, t)\rangle - |f_i^{(eq)}(\mathbf{r}, t)\rangle). \tag{3.45}$$

Here bra $\langle|$ and ket $|\rangle$ vectors are used to denote row and column vectors, respectively. The number Q of different velocities of the model defines the dimensions of the vectors (Q) and the matrix S (Q×Q). The LBGK models appear as special cases when the relaxation times are all equal and the collision matrix is $S = (1/\xi)I$ with I the identity matrix.

The general MRT collision process is accomplished in the space spanned by the eigenvectors of the collision matrix S, and the corresponding eigenvalues are the inverses of the relaxation times. Q moments m_j of distribution functions f_i can be obtained as [22]

$$m_j = \langle \phi_j | f \rangle = \langle f | \phi_j \rangle, \tag{3.46}$$

where $|\phi_j\rangle$ are eigenvectors of S. The velocity and moment spaces are related by a linear mapping M: $|m\rangle = M|f\rangle$ and $|f\rangle = M^{-1}|m\rangle$ The evolution equation Eq. (3.45) of the MRT model becomes [20–22]

$$|f_i(\mathbf{r} + \lambda \mathbf{c}_i, t + \eta)\rangle - |f_i(\mathbf{r}, t)\rangle = -M^{-1}\hat{S}(|m_i(\mathbf{r}, t)\rangle - |m_i^{(eq)}(\mathbf{r}, t)\rangle), \tag{3.47}$$

where we have introduced a diagonal collision matrix $\hat{S} = M \cdot S \cdot M^{-1}$ and the equilibrium value $m_i^{(eq)}$ of the moment m_i. Using the fact that $(M \cdot M^T)$ is a diagonal matrix with diagonal elements $\langle \phi_j | \phi_j \rangle$, Eq. (3.47) can now be written as [22]

$$|f_i(\mathbf{r} + \lambda \mathbf{c}_i, t + \eta)\rangle - |f_i(\mathbf{r}, t)\rangle = -\sum_j \frac{s_j}{\langle \phi_j | \phi_j \rangle} [m_j(\mathbf{r}, t) - m_j^{(eq)}(\mathbf{r}, t)] |\phi_j\rangle. \tag{3.48}$$

A set of values for the vectors $|\phi_j\rangle$ and matrices $\hat{S}$, M and $M^{(eq)}$ are given in Ref. [22] for the three-dimensional models D3Q15 and D3Q19. Both these models have common moments corresponding to physical quantities like mass density, momentum, the part of kinetic energy independent of density, the energy flux independent of mass flux and the symmetric traceless viscous stress tensor. In addition, in the D3Q15 model there is an antisymmetric third-order moment, while in the D3Q19 model, there are five additional conserved vectors [22].

An important consequence of the MRT model is the maximum number of adjustable relaxation times, one for each class of kinetic modes invariant under the symmetry group of the underlying lattice. Also, there is some freedom in the construction of the equilibrium functions of these non-conserved moments. One result of using MRT instead of LBGK appears to be improved numerical stability [21, 67], which together with the other advanced features, is important in *e.g.* high Reynolds-number simulations. In simulations of fluid flow in porous materials, however, the improvements the MRT model provides, do not usually play a very important role, because even the relatively simple realizations of the LBGK model have been found to produce adequate hydrodynamics in simulations of creeping flow in complex structures, where the interest is usually to find averaged quantities like the permeability. The LBGK models have some features that need special attention, and on the

other hand, at least one of these can be also beneficial: the dependence of permeability on the relaxation parameter of the LBGK model can be used to reduce finite-size errors (see Secs. 3.4.1 and 3.5.1). A corresponding dependence does not exist in the MRT model.

3.4 Boundary conditions and forcing terms

3.4.1 No-slip condition

The physical boundary condition at solid-fluid interfaces is the no-slip condition, which in lattice-Boltzmann simulations is usually realized by the so-called bounce-back rule [68,69]. In this approach the momenta of the particles that meet a solid wall are simply reversed. Bounce back can be applied either at wall points or at halfway of the links between the fluid and solid points. In stationary flow these approaches are equivalent, though in bounce back at the wall points, the particles need to travel a double distance and spend a double time during the bounce-back event in comparison with the bounce back in the links. On the other hand, this property can be used to enhance the numerical stability by decreasing fluctuations caused by parity invariance [70].

The quality of the bounce-back condition for the lattice-Boltzmann method has been discussed *e.g.* in Refs. [68, 71–73]. In a simple shear flow the bounce-back condition assumes that the location of the wall is exactly at halfway between the last fluid point and the first wall point. In more complicated cases the no-slip boundary lies somewhere in between these two points, the exact place depending on the geometry of the system, the relaxation parameter ξ of the LBGK model [69, 71] and the realization of forcing term [74, 75]. In Poiseuille flow, *e.g.*, the bounce-back rule with body-force (Sec. 3.4.2) gives velocity fields that deviate from the exact solution by [76]

$$\Delta u = u_{\max} \frac{48\nu^2 - 4\nu - 1}{W^2}, \tag{3.49}$$

where $u_{\max}$ is the velocity at the center of the channel, and W is the channel width (in lattice units). Hence the flow simulated with the LBGK model will in this case depend somewhat on viscosity, especially at low discretization levels.

In addition to the bounce-back condition, several authors have proposed more sophisticated, so-called second-order boundaries, which model a no-slip boundary exactly at the wall nodes. Many of these are restricted to regular geometries, like octagonal objects and flat walls [59, 73], but there are also general boundary-fitted models [77, 78] available. For practical simulations the bounce-back boundary is however very attractive, because it is a simple and computationally efficient method for imposing no-slip conditions on irregularly shaped walls. Also, the error created by the bounce-back boundary does not destroy the spatial second-order

convergence of the method [71,79].

3.4.2 Body force

In simulating fluid flow it is important that the velocity and pressure boundary conditions of the system have been imposed in a consistent way. Proper velocity and pressure boundaries have been proposed *e.g.* in Refs. [79–81]. As for an incompressible fluid an external force and a pressure gradient have an equal contribution in the Navier-Stokes equation Eq. (2.6), it is often possible to use in this case a uniform body force [24, 28, 71, 82, 83] instead of pressure or velocity boundaries. The use of body force is based on the assumption that the pressure gradient induced by an external pressure difference is approximately constant in the system. Conditions that are very close to pressure boundaries can be obtained by averaging the velocity and pressure fields over the planes of the inlet and outlet of the simulated system [71]. The pressure field generated by the body force can be obtained from the effective pressure p_{eff},

$$p_{\text{eff}}(\mathbf{r}, t) = c_s^2 \Delta\rho(\mathbf{r}, t) - \bar{\rho} g x, \tag{3.50}$$

where x is the distance from the inlet of the system measured in the flow direction, and g is the acceleration the body force gives to the fluid.

In the lattice-Boltzmann method body force is simulated by adding at each time step a fixed amount of momentum to all lattice points within the void space. This can be done in several ways, *e.g.* by adding the momentum to links with nonzero projection in the direction of the force, taking into account the weights m_i of the links. The momentum oscillates during one time step because of applying bounce back and body force, which needs to be considered also in determining the actual hydrodynamic quantities. One simple treatment is to add half of the momentum before and half after the collision phase. The body force approach is exact in simple tube flow, and in more complicated geometries it is supposed to work best for small Reynolds numbers, when nonlinear effects in the flow are small. However, for high Reynolds-number flows, and for more complicated boundary conditions, explicit velocity and pressure boundaries or improved versions of forcing term may be needed. Due to discrete-lattice effects, the second-order spatial convergence may be violated close to the solid boundaries, which could be taken into account when introducing a force in the lattice-Boltzmann equation. Several techniques for properly dealing with this problem were reported in Refs. [74, 75, 84]. Notice that improved versions of body force and sub-grid scale boundary conditions cause *e.g.* changes in Eq. (3.49).

3.4.3 Moving fluid-solid boundaries

If solid particles are suspended in the lattice-Boltzmann flow, they are obviously defined by a boundary surface, which cuts some of the links between lattice nodes. The fluid particles moving along these links interact with the solid surface at the boundary nodes, which can be realized in several different ways [29, 30, 85]. The no-slip boundary condition can be realized on the boundary nodes with respect to the velocity, determined by the velocity, angular velocity, and centre of mass (or mass distribution) of the particle. In addition to the bounce-back rule the velocity distributions that meet the wall experience a change of momentum [29],

$$\Delta f_i = 2b_i \bar{\rho} \mathbf{u}_w \cdot \mathbf{c}_i, \tag{3.51}$$

where $\bar{\rho}$ is the mean density of the fluid, $\mathbf{u}_w$ is the velocity of the particle, and $b_i = m_i/c_s^2$ is a coefficient in the equilibrium distribution (Eq. (3.43)). A simple special case of a moving fluid-solid boundary is a moving wall, in which the only additional condition is given by Eq. (3.51). If the boundary surfaces change their places, fluid must be removed from ahead of and created behind the particles [30]. Another approach that has been found to work as well uses particles which include fluid [29, 84]. The effects caused by fluctuating shape of the moving particles have dealt with applying various boundary conditions, such as relaxed bounce-back rule [85], continuous bounce-back rule [86] or second-order boundary conditions [87].

3.5 Error sources

In addition to the unavoidable errors, as in all numerical methods, related to the discreteness of the computational grid, the numerical quality of lattice-Boltzmann simulations is mainly affected by finite-size effects, compressibility errors and boundary effects [8, 59, 71–73, 79]. Moreover, elimination of staggered invariants may sometimes need extra care, and if there are diagonal leak flows in the lattice used, they may cause a detectable effect near the percolation threshold in the case of flow in a porous medium. The leak flows can however be removed by applying an appropriate bounce-back rule, if necessary. In practice it is not always easy to separate the errors caused by these various effects, but the total error can often be estimated by simulating the problem for several system sizes.

3.5.1 Finite-size effects and shift of the boundary

Finite-size effects are caused by the limited number of grid points in the calculational lattice. They are often the main error source in lattice-Boltzmann simulations. With respect to these effects, the largest possible size of lattice spacing is determined

by the needed accuracy of the simulations. The magnitude of these effects can be estimated by simulating the system for several system sizes, but occasionally it can be difficult to distinguish the finite-size effects from other sources of numerical error. These effects restrict to some extent the use of the lattice-Boltzmann method. In porous media close to the percolation threshold, *e.g.*, many pores are very small, and very big lattices may be needed for realistic simulations. Also, it is not always clear whether the finite-size effects are dominated by the minimum pore size, or could sometimes the average pore size be more important. Some improvement in this respect would be provided by refined, non-uniform grids [12,71,76,88].

Practice has shown [28,89] that smaller values of the BGK relaxation parameter ξ tend to decrease the finite-size effects because of the shift of the no-slip boundary. Equation (3.49) can be used to explain this: low-discretization simulations regularly give too high flow velocities, whereas decreasing ξ has the opposite effect down to $\xi = 0.625$, at least for tube flows. On the other hand, as discussed above, too small values of ξ may introduce some error in the lattice-Boltzmann simulations [9].

3.5.2 Lattice discreteness

A regular lattice used in simple lattice-Boltzmann models leads to quite rough surfaces for non-flat fluid-solid boundaries. Fluid, however, tends to "smooth out" rough surfaces [71,90]. In lattice-Boltzmann simulations this smoothing out can *e.g.* be seen in the values of the hydrodynamic radii of various obstacles. The hydrodynamic radius of an obstacle can be derived by simulating fluid flow in an infinite array of such obstacles [29,71]. For example, flow past a cubic array of spheres has become a reference system for hydrodynamic algorithms because accurate reference values for the permeability, and the drag coefficient, are available over a wide range of porosities [91,92]. When describing a sphere in a lattice, there is a range of radii which correspond to the same discretized object, for instance radius values between $\sqrt{2}$ and $\sqrt{3}$. Thus a reasonable and well-defined measure of the size of the object is its volume, and the radius of the equal-volume sphere, *i.e.* the hydraulic radius [33], which for spheres has actually found to be very close to the measured hydrodynamic radius [29]. The apparent roughness of the surface does not necessarily have a big effect on the accuracy of the simulations, but hydrodynamic radius may depend quite strongly on ξ in the LBGK models.

3.5.3 Staggered invariants

Unphysical conserved quantities, *i.e.* spurious invariants, can create unphysical hydrodynamic modes in the simulated system, and they should usually be eliminated from the model [8]. In all lattice-Boltzmann models the discrete nature of the system creates a class of spurious invariants, called the staggered invariants [9,29,93]. They depend on the parity of space and time, and may play an important role in

the physical behaviour of the lattice-Boltzmann models because they are coupled to the nonlinear terms in the Navier-Stokes equation [9, 93]. Due to the staggered invariants, *e.g.* the fluid momentum may oscillate in a time scale of a few time steps even in a stationary state [II, 9]. In open areas this effect is usually unimportant, but in flows generated by a body force this effect may become visible in closed pores, as the fluid momentum may oscillate around zero with a magnitude determined by the body force. The influence of staggered invariants can, however, be minimized by properly choosing the initial condition of the fluid particles [9, 93]. Spatial or temporal averaging can also be used to reduce them [29], and, especially in a stationary state, staggered momenta can be eliminated by averaging the quantities over a few time steps.

Due to the discreteness of the models, there are also other spurious invariants that are characteristic for particular models. For example, in the D3Q14 and D3Q15 models fluid points are not directly connected to their next-nearest neighbours, and fluid momentum may form unphysical regular patterns (checkerboard effect [22, 71]). Similar spurious invariants are also found in other lattice-based methods, *e.g.* in the HPP lattice-gas model [15].

3.5.4 Compressibility errors

Compressibility errors are caused by the dependence of pressure on density (Eq. 3.44), which violates the assumption of incompressible fluid in the lattice-Boltzmann method. Simulating incompressible fluid with a compressible lattice-Boltzmann fluid necessitates the use of low Mach numbers (*i.e.* the ratio of the mean speed of fluid to the speed of sound). The compressibility errors in the lattice-Boltzmann methods are typically small fluctuations in the density associated with variations in the pressure. Many fluid flows computed by the LBGK sceme may have pressure oscillations of a wavelength of a few lattice spacings. With increasing Reynolds and Mach numbers they can become pronounced and even prevent the flow to converge. The practical upper limit for speed is about 0.1 in the LBGK models, and about 0.2 [22] in the MRT models for which pressure oscillations can also be reduced [21, 22, 67]. Notice that in applying the body force or moving particles (see Sections 3.4.2 and 3.4.3), use of the average fluid density instead of the local density tends to decrease the fluctuations in the pressure [94]. In two dimensions the compressibility of the fluid can be eliminated for stationary flows [95].

In simulations the compressibility of the fluid can also cause large-scale fluctuations that appear *e.g.* as pressure waves that become noticeable especially in large void spaces. To some extent they are often present in typical porous-material simulations that use the body force. The effective pressure depends on the fluid density according to Eq. (3.50), and if the initial state has a constant density, pressure waves are generated in large pores in the direction of the body force. Very large void spaces may exist at an uneven surface of the material sample and pressure waves created

there may considerably slow down the saturation. To reduce this effect in practice, the flow problem can be solved by applying the body force only in the inner points of the sample.

3.6 Implementation of the lattice-Boltzmann method

3.6.1 Practical computational requirements

In practice, it is convenient to represent the computational lattice by floating-point numbers that are responsible for the main memory usage of the method. For example, when 32-bit floating-point numbers are used in the D3Q19 model, one lattice site requires 76 bytes. Realistic simulations thus require large amounts of computational resources, and are often executed on parallel systems. Continuous development of computers has however made it possible to perform quite realistic 3D simulations that typically require gigabytes of core memory, even in workstations and personal computers.

Large simulation lattices require tens of gigabytes of core memory, and such memory is still available only in supercomputers. These large simulation lattices may also require weeks of simulation time in terms of single-processor hours. Techniques to optimize the single-processor performance of lattice-Boltzmann codes are reported *e.g.* in Refs. [96, 97]. Fortunately, the inherent spatial locality of the lattice-Boltzmann updating rules makes these methods ideal for parallel processing, and simulation times can be reduced by nearly inversely proportional to the number of processors used.

3.6.2 Saturation time

The time used by lattice-Boltzmann simulations is usually taken up mainly by repeated identical timesteps. After a timestep is optimized, the speed of a simulation can still be increased by decreasing the amount of the necessary timesteps.

In permeability simulations, a dimensional analysis shows that, with a constant body force, the saturation time t_{sat} needed to reach the steady state is of the form [73]

$$t_{\mathrm{sat}} \propto R_{\mathrm{pore}}^2/\nu, \tag{3.52}$$

where R_{pore} is the characteristic length of the void pores in the system and ν is the kinematic viscosity of the fluid. With a constant body force, saturation times can be very long for systems of high porosity. In practical simulations sometimes tens of thousands of time steps may be needed. Reaching the steady-state solution with a constant body force may thus be computationally inefficient.

Accurate initial conditions are needed in time-dependent flows [59], whereas in time-independent flows properly chosen initial conditions may be used to speed-

up the saturation. Such a condition can sometimes be found by keeping constant an essential dimensionless number, like the Reynolds number. Simulation time will be smaller than in the original system, if, *e.g.*, the simulation is carried out first on a smaller lattice, or at a clearly higher viscosity.

The saturation time can also be reduced by using the iterative momentum-relaxation (IMR) method, where the applied body force is adjusted during the iteration in a definite relation to the change of the fluid momentum during iteration steps [71]. Several other approaches have also been introduced to efficiently find the steady-state solution of the lattice-Boltzmann method [98]. In some methods of computational fluid dynamics this problem can be overcome by solving a time-independent flow instead of the complete Navier-Stokes equation.

3.6.3 Sample boundaries

In fluid-flow simulations the boundary conditions on the sample boundaries may have significant effect on results. The problem is similar as in experiments, but in the simulations the boundaries can be implemented accurately and consistently, as far as the used algorithms are adequate. Often the boundary conditions are chosen to mimic the experiments to gain comparability, and for this purpose the no-slip, slip [11] or periodic boundary conditions are usually applied on the lateral boundaries parallel to mean flow. These all can be implemented reliably in the lattice-Boltzmann method, and also *e.g.* open boundaries for hydrodynamic models have been proposed [99].

In permeability experiments typical boundary conditions at the inlet and outlet of the sample is that they are in contact with free fluid under the given pressures, *i.e.* the actual pressure boundaries lay relatively far from the sample surfaces. In numerical simulations a corresponding condition is obtained by adding free fluid layers next to the inlet and outlet.

3.7 Benchmark studies

Various benchmark tests can be used to estimate the accuracy of lattice-Boltzmann simulations. In this section we introduce selected studies in which the error sources (see Sec. 3.5), at least to some extent, can be considered independent of each other. We show the boundary effects in a Poiseuille flow and demonstrate in simple cases the importance of the effects of discrete lattice. Finally we show, with examples of porous materials, how discretization level and thickness of free fluid layer appear in practical permeability simulations. Especially we point out the necessity of simulations for several voxel sizes to estimate the error caused by discretization.

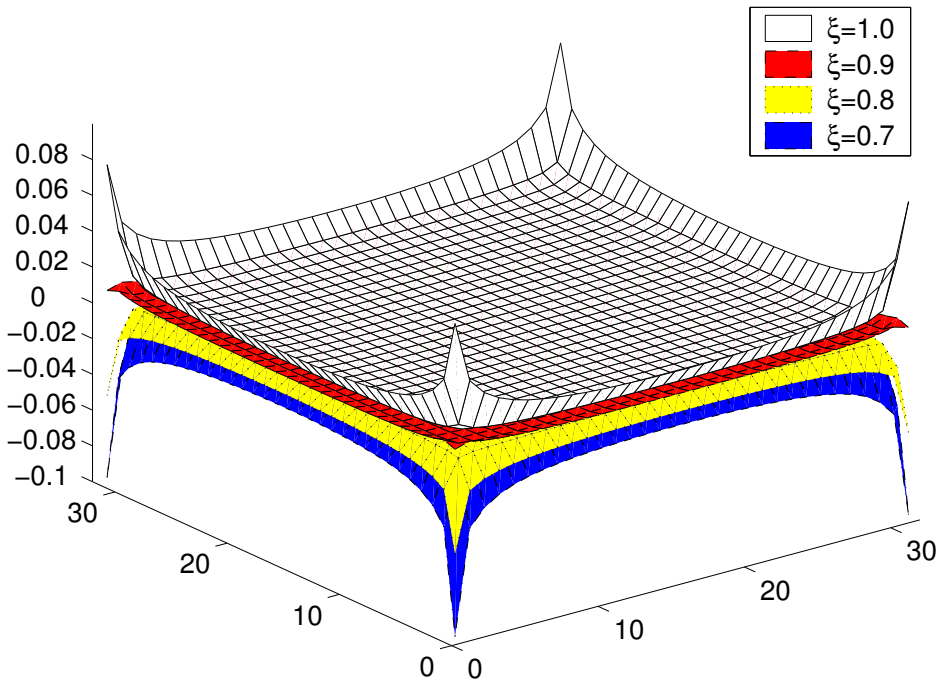

FIGURE 3.3 Relative error of the numerical solution of the Stokesian velocity field for a Poiseuille flow through a tube with quadratic cross section of size 32 lattice points. The surfaces from down to up show the solutions from $\xi = 0.7$ to $\xi = 1.0$. The reference values are calculated from the analytical solution given in Ref. [100].

3.7.1 Poiseuille flow: Tube with square cross section

One of the few cases for which an analytical solution of the the basic hydrodynamic equations is known is Poiseuille flow, flow through a linear tube with constant cross section. We used here a tube with square cross section because then the geometry can be discretized on a cubic lattice without discretization error. We considered a tube directed along the x direction with a square cross section of a side length of 32 lattice points, and compared the velocity component $v_x(y, z)$ with its exactly known reference value $v_x^{\text{ref}}(y, z)$ given in Ref. [100].

Figure 3.3 shows the relative error $(v_x - v_x^{\text{ref}})/v_x^{\text{ref}}$ for the LBGK solution with a varying relaxation parameter ξ. Around the center of the tube the analytical flow profile is very well recovered in terms of the relative error. Near the boundaries we find deviations which are biggest in the corners. The solution with $\xi = 0.7$ underestimates the reference value v^{ref} while the solution with $\xi = 1.0$ overestimates the true value. Hence, the relaxation parameter ξ or equivalently the viscosity ν could be used to fit the numerical results to the analytical velocity field. From Fig. 3.3 one expects to find a value $0.8 < \xi < 0.9$ for which the numerical solution closely matches the analytical velocity profile for this flow system. We find that these relative error result mainly from boundary effects that extend to a few lattice spacings away from

the boundaries.

3.7.2 Cubic array of spheres

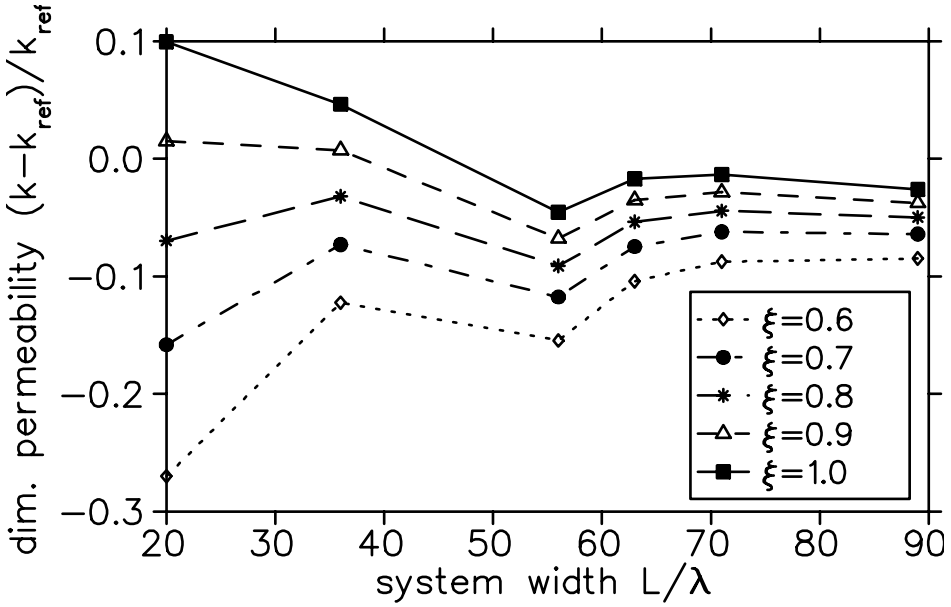

FIGURE 3.4 Numerical results for the dimensionless permeability $(k - k_{ref})/k_{ref}$ of a cubic array of spheres for different values of dimensionless system width L/λ with λ the lattice spacing, and for various relaxation parameters ξ. The porosity is constant for all systems, $\phi = 0.15$. The reference value $k_{\rm ref}$ is taken from Ref. [91].

To test the accuracy of the LBGK method in a more complicated geometry with narrow constrictions, we computed flow past a cubic array of spheres. This problem has become a reference system for checking hydrodynamic algorithms because accurate reference values for the permeability and the drag coefficient are available over a wide range of porosities [91, 92].

The solution of this problem proceeds by solving the problem in a single unit cell of the cubic lattice. We generated six different unit cells of sizes (L) $20, 36, 56, 63, 71$ and 89 lattice spacings λ. A sphere is placed at the center of the cell with radius chosen such that the porosity matches as close as possible to $\phi = 0.15$. Thus, the porosity is close to that of the sandstone investigated below. Once the velocity field was known, the permeability was calculated from Eq. (2.12), and the expression [91]

$$\frac{k}{R^2} = \frac{1}{6\pi C_D}\left(\frac{L}{R}\right)^3 \tag{3.53}$$

was utilized to obtain a reference value $k_{\rm ref}$ for the permeability from the drag coefficient C_D given in Ref. [91]. The radius $R(\phi, L)$ of the sphere is given implicitly by

the expression

$$\phi = \frac{8\pi}{3}\left(\frac{R}{L}\right)^3 - 3\pi\left(\frac{R}{L}\right)^2 + \frac{\pi}{4} + 1 \quad . \tag{3.54}$$

To calculate the reference value k_{ref} we solve this equation, and find $(L/R) \approx 1.6011$ for $\phi = 0.15$. Using the drag coefficient $C_D = 1.020 \times 10^3$ [91], we find $k_{\mathrm{ref}}/R^2 \approx 0.0002135$. In Fig. 3.4, which display results of the lattice-Boltzmann simulations, the relative error $(k - k_{\mathrm{ref}})/k_{\mathrm{ref}}$ of the permeability k is plotted as a function of the linear dimensionless system size L/λ. With increasing resolution the results converge and the error predominantly decreases. The curves in Fig. 3.4 do not behave monotonously, and we would expect the discrepancy between the simulation results and the reference value to result mainly from discretization errors. The curve that displays the discretized cross-sectional area of the smallest voids in the structure as a function of L/λ shows a similar nonmonotonic behaviour.

3.7.3 Randomly placed spheres

If the fluid-solid boundaries move, as is the case in suspension simulations, the lattice description of the particle varies. In such cases the discreteness can be taken into account by averaging the hydrodynamic radius over a large sample of randomly placed particles. Examples of the averaged hydrodynamic radii a_0 for 2D spheres with $\xi = 1.0$ [29] are shown in Table 3.1, and corresponding values for 3D spheres [29] are shown in Table 3.2.

TABLE 3.1 The actual radii a_0 and the averaged hydrodynamic radii a for randomly placed 2D spheres; $\xi = 1.0$.

a_0	1.5	2.5	4.5	8.5	16.5
a	1.36	2.43	4.49	8.53	16.54

TABLE 3.2 The actual radii a_0, the radii of the equal-volume spheres a_v, and the averaged hydrodynamic radii a for randomly placed 3D spheres; $\xi = 1.0$.

a_0	1.5	2.5	4.5	8.5
a_v	1.66	2.68	4.53	8.48
a	1.54	2.61	4.53	8.47

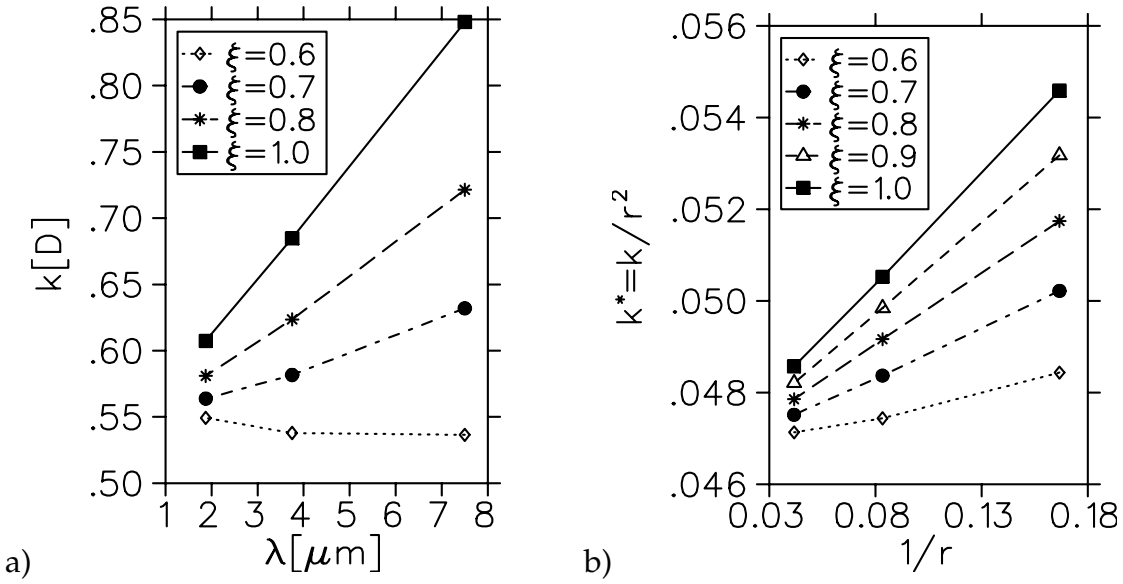

FIGURE 3.5 a) Permeability k of a tomographic image of the Fontainebleau sandstone for different values of lattice spacing λ and different relaxation parameters ξ. The resolution of the original sample is 7.5 μm. b) Dimensionless permeability $k^* = k/r^2$ of a modelled wire for different values of yarn radius r (in lattice units) and different relaxation parameters ξ.

3.7.4 Fine graining

In order to get rid of the discretization errors, such as seen *e.g.* in Fig. 3.4, we investigate the permeability of samples with a fine graining algorithm that replaces each lattice point by $n \times n \times n$ lattice points of the same phase with $n = 2, 3, 4, \ldots$. With this algorithm *e.g.* the porosity and specific surface area are conserved. Fig. 3.5 a) shows permeability $k^{(n)}$ for a small sample of a tomographic image of Fontainebleau sandstone [II] (porosity $\phi \approx 0.15$), and Fig. 3.5 b) shows permeability of a modelled wire [101] (porosity $\phi \approx 0.5$). The dependence of permeability on the LBGK relaxation parameter ξ (see Sec. 3.5.1) is pronounced at low resolutions, and the effect is stronger with sandstone than with wire. Generally this dependence is pronounced if there is a lot of small pores and narrow flow channels in the sample. Usually, for given type of material, higher discretization level is needed for low-porosity samples. Occasionally there are also other case-specific factors than porosity for different types of media. At least for regular homogeneous materials, such as wires, the representative length scale of flow channels should be over about five lattice spacings to gain a reliable hydrodynamical behaviour (cf. Knudsen flow effects of real fluid, Eq. (2.1)). This kind of test is thus needed in practical permeability simulations to estimate the effect of resolution for used relaxation parameter ξ.

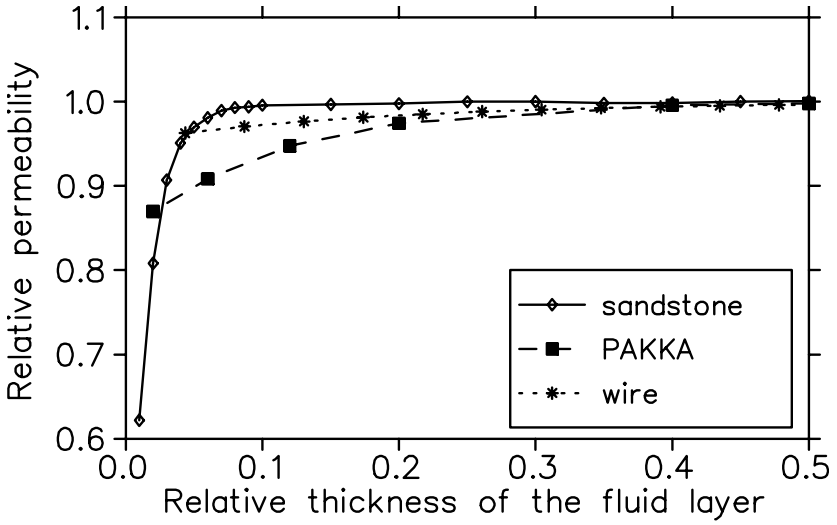

FIGURE 3.6 The effect of the thickness of free fluid layer on simulated permeability. Shown are scaled permeability as a function of the thickness of free fluid layer divided by the thickness of sample. Used samples are a modelled wire, a PAKKA-model sample and a tomographic image and of Fontainebleau sandstone.

3.7.5 Effect of free fluid layer

As discussed in Sec. 3.6.3 an undisturbed fluid flow at the inlet and outlet is obtained by adding free fluid layers next to these sample boundaries. The effect of the thickness of this fluid layer is shown in Fig. 3.6 for several different samples. Used samples are a modelled wire [101], early PAKKA-model sample (shown on the left in Fig. 4.6 [102]) and a tomographic image and of Fontainebleau sandstone (Fig. 4.11 [103]). In these simulations a body force and periodic boundary conditions were used, and the LBGK-relaxation parameter was $\xi = 1.0$.

For thin layers of free fluid the simulated permeabilities are reduced as a result of additional resistance present at the narrow inlet and outlet. For increasing layer thickness permeability saturates depending on properties like porosity, relative thickness of the porous sample and structure of the inlet and outlet. In this context the relative thickness is the ratio of thickness to a representative size of pores and obstacles in the sample. The modelled wires had quite a small relative thickness, but they had high porosity and consisted of round yarns, which made the flow resistance at the inlet and outlet fairly small. Therefore the effect of thickness of the fluid layer was not very big. On the other hand, in the sandstone the porosity was $\phi = 0.15$ and the evenly cut inlet and outlet induced a fairly high flow resistance. Therefore the relative permeability of the sandstone sample was reduced more than that of the other test samples for decreasing free fluid layer (cf. Fig. 3.6). The effect of the thickness of the free fluid layer on the permeability was found to be typically of the order of a few per cent.

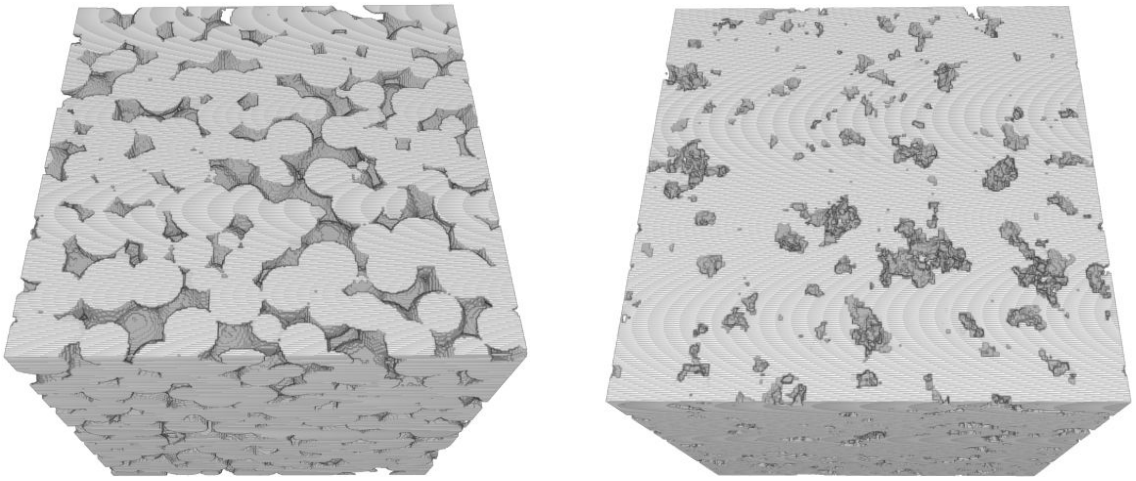

FIGURE 3.7 Diagenesis model (left) and simulated annealing model (right) constructed of a tomographic image of Fontainebleau sandstone shown in Fig. 4.11.

3.8 Samples of porous media

3.8.1 Modelling

One often needs to model samples of porous media to be used in fluid-flow simulations. For example, in oil recovery an important problem is to deduce the pore-space structure of sandstone by indirect methods, as obviously it is not always possible to directly measure the three-dimensional structure. Small samples of a linear size of one millimeter can be measured by tomographic imaging using x-rays. These samples can then be used to test *e.g.* pore structures constructed based on measured properties such as porosity, specific surface area and two-point correlation functions. The basic problem then is to evaluate in some way the quality of the constructed pore structures with respect to the real measured structure.

In sandstone modelling *e.g.* the main geological sandstone-forming processes [104] have been numerically modelled by the diagenesis model [103]. This model uses some properties of the original sandstone obtained by analyzing backscattered electrons/cathodo-luminescence images. They provide input data such as porosity, grain size distribution, a visual estimate of the degree of compaction, the amount of quartz cement, clay contents and texture. Diagenesis modelling of sandstone is carried out in three main steps: grain sedimentation, compaction and diagenesis.

Another approach for sandstone modelling is the simulated annealing algorithm [103] that has been employed to generate a stochastic model for Berea and Fontainebleau sandstone. These models have acquired the status of a reference standard for modelling and analysis of sedimentary rocks [41,44,105]. The simulated annealing algorithm uses for each sample a prescribed two-point probability function, linear-path function and pore-size distribution function [31,103,106]. In Fig. 3.7 we show samples generated with these models.

Similarly models are used in simulating various aspects of paper material, *e.g.* the numerical PAKKA model [102,107]. It is used to produce three-dimensional random networks of fibres, which can be considered as a model of paper-like materials. In this model fibre webs are grown by randomly depositing flexible fibres of rectangular cross section on a flat substrate. These webs are periodic in the in-plane directions. The surfaces in the perpendicular direction have a somewhat different structure from that in the bulk of the material due to boundary effects in the deposition process, and are therefore usually removed in order to obtain homogeneous structures. The porosity of the samples appears [102] to only depend on and can thus be controlled by varying the flexibility of the deposited fibres. Utilization [I, V, 89] of PAKKA model is reviewed in Sec. 4.4. Other examples of the models of fibrous porous structures, which can also be used to analyze the elastic properties of these structures, are given *e.g.* in Refs. [101,108].

3.8.2 Tomographic imaging

X-ray computed microtomography ($X - \mu CT$) is a fairly novel technique used for three-dimensional imaging of materials. This method has been applied *e.g.* in analysing the structure of paper and sandstone. $X - \mu CT$ consists of obtaining a large set of images while passing radiation through the sample at different angles. The projected images can be combined so as to reconstruct the geometry of the interior structure. In practice, the equipment involves at least a microfocus x-ray source, a CCD camera and a computer to unload the CCD array.

The quality and resolution of the obtained images depend *e.g.* on the size of the focus of the x-ray beam, the amount of pixels in the CCD camera, and the image reconstruction techniques. The resolution can be adjusted to some extent by moving the object between the x-ray source and the camera. In general, high-resolution images are obtained by keeping the object close to the source and far from the camera. They represent small volumes physically, limited by the amount of pixels in the camera and computational requirements. The wavelengths of the available x-rays are not usually a limiting factor in the resolution. In the construction of a 3D image, the amount of separate 2D images needed is typically of the order of a couple of hundred, and the time consumption per one image can be from a few seconds to tens of minutes.

Recent research in this area has produced different applications and modifications of the x-ray microtomography techniques providing images of varying quality and resolution [IV, 43, 109]. The traditional image reconstruction technique is the absorptive-contrast method [43] used *e.g.* in medical applications. The density sensitivity of this method can be used to distinguish different material components and thus to analyze them separately.

For paper in which cellulose and other material components have very similar absorptivities for x-rays, instead of the absorptive-contrast method, the phase-

contrast method is preferred [109–112]. In this method images are produced by low-energy monochromatic radiation, and the resolutions obtained have now reached the sub-micrometer regime [IV].

Chapter 4

Fluid-flow simulations in porous media with the lattice-Boltzmann method

4.1 Resolution and size of tomographic images of paper

X-ray microtomography combined with suitable numerical tools allows visualisation and characterisation of structural properties of paper and board in three dimensions. One of the most important questions here is whether the recent imaging techniques are capable of giving images of sufficient quality and resolution to enable a reasonable quantification of 3D structural characteristics.

Samples of different paper grades were imaged using both high- and low-resolution $X - \mu CT$ techniques. 3D structural characteristics and fluid-transport properties of these images were measured with image analysis techniques and the lattice-Boltzmann method. Of particular interest were the effects on the computed results of the finite size of the samples and of the image resolution, the latter of which also specifies the computational grid used in the numerical simulations.

4.1.1 Materials and methods

Three different paper samples, namely filter paper, newsprint and hand sheets, were chosen to test the applicability of $X - \mu CT$ techniques. The hand sheet was made of bleached softwood kraft pulp of spruce. The newsprint was made of thermo-mechanical pulp of spruce in a commercial paper machine, and the paper was not calendered. The filter paper was a commercial circular black ribbon filter paper made of cotton linters. In Table 4.1 we show the thickness, density and basis weight of the imaged paper samples. The accuracies of these quantities are typically of the order of a few per cent, and hence the chosen samples have clearly different

TABLE 4.1 Bulk properties of the imaged paper samples.

Sample	Thickness (μm)	Density ($\mathrm{kg/m^3}$)	Basis weight ($\mathrm{g/m^2}$)
Hand sheet	98	647	63.4
Newsprint	109	403	44.1
Filter paper	158	486	76.7

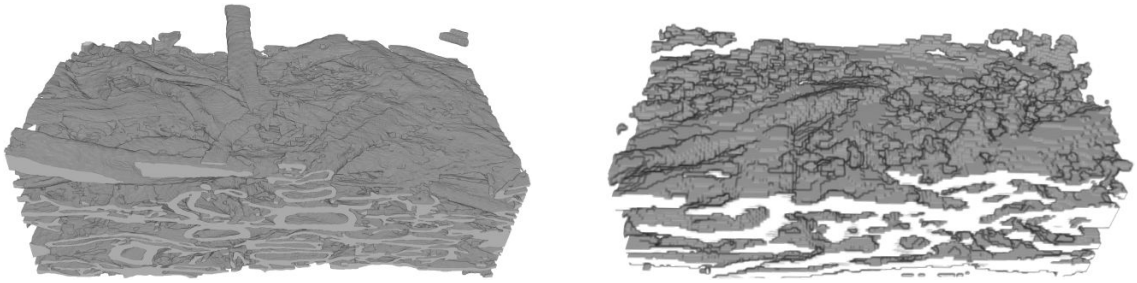

FIGURE 4.1 High- (left) and and low-resolution (right) images of newsprint paper.

characteristics and are expected to give distinct results in image analysis and fluid-transport simulations.

In order to identify the necessary level of structural details for a reliable characterisation of different paper grades, the samples were imaged using high- and low-resolution $X-\mu CT$ techniques. In Fig. 4.1 we show high- and low-resolution images of newsprint paper. Due to the limited computational resources, relatively small image sizes, below $0.1\ \mathrm{mm}^2$, were used in the high-resolution and several low-resolution images. Also a set with a larger image size, about $1\ \mathrm{mm}^2$, was taken with the low-resolution technique. The low-resolution images were obtained using polychromatic radiation [43] (resolution $\approx 5\ \mu\mathrm{m}$, voxel size $2\ \mu\mathrm{m}^3$) and the high-resolution images were obtained using monochromatic synchrotron radiation in the phase-contrast mode [109] (resolution $\approx 1\ \mu\mathrm{m}$, voxel size $0.35\ \mu\mathrm{m}^3$). The low and high-resolution images were reconstructed and processed according to the routines given in Refs. [43] and [113], respectively. Small detached volumes of fibrous and porous phases were removed by a 3D filtering technique, and the surfaces of the samples were defined using the rolling-ball algorithm [114, 115]. According to this algorithm surface is defined by the route of a ball with a suitable radius that rolls along the surface. This method allows the detection of the main structures of uneven surfaces, the interior pores excluded.

Image analysis techniques [32, 43] were used to measure 3D structural characteristics such as porosity, specific surface area, hydraulic pore-radius distribution and diffusive tortuosity in the principal directions [IV]. The diffusive tortuosity measurements were based on 1000 successful paths of a random-walk simulation through the paper volume with a random starting point on an appropriate volume

TABLE 4.2 Some material properties obtained from the 3D images of the samples: Thickness T, density ρ, basis weight Bw, porosity ϕ and specific surface area SSA.

Sample	Image size	Resolution	T (μm)	ρ (kg/m^3)	Bw (g/m^2)	ϕ (%)	SSA ($\times 10^3$/m)
Hand sheet	Small	High	90.1	829	74.9	46.4	303
	Small	Low	88.5	857	75.5	44.9	179
	Large	Low	101.5	796	79.6	49.0	176
Newsprint	Small	High	99.3	655	65.1	57.7	387
	Small	Low	119.2	651	76.1	58.2	179
	Large	Low	115.7	655	74.3	58.0	181
Filter paper	Small	High	190.9	550	105.5	64.3	234
	Small	Low	181.6	641	116.2	58.7	164
	Large	Low	179.4	570	101.8	63.4	157

edge. The values were measured in the principal directions. Moreover, such flow-related material parameters as the tortuosity of the flow paths and the flow permeability in the transverse direction, defined by Eqs. (2.17) and (2.12), respectively, were computed using direct numerical simulations with the lattice-Boltzmann method. We used a specific 19-link LBGK model with a uniform external body force and the bounce-back boundary condition at the solid-fluid interfaces (see Secs. 3.3, 3.4.1 and 3.4.2). In order to ensure an unrestricted fluid flow at the inlet and outlet (see Sec. 3.7.5), a free fluid layer with a thickness of about 10 % of the sample thickness was added on top of the sample, and periodic boundary conditions were implemented in all outer boundaries of the rectangular computation volume.

4.1.2 Detection of solid material

In order to compare the ability of the imaging techniques to detect the correct amount of material in the imaged volumes, the quantities of Table 4.1 (thickness, density and basis weight) were also estimated by image analysis. We show the results in Table 4.2 together with porosity and specific surface area. Here and in the following, the values of low-resolution samples are mean values obtained for available replicate samples.

The slight differences between the bulk properties and the image analysis results arise in part from normal variation, *i.e.* are related to the so-called formation of the samples used, but also from the difference between the standard thickness (ISO 534:1988) and the rolling-ball-defined thickness, and from a probable overestimation of the density of fibres (1550 kg/m^3) used in Table 4.2 for all paper grades [IV]. In addition, the used techniques may overestimate the volume of the solid material in the images. The specific surface area for the low-resolution images is consistently

TABLE 4.3 Tortuosity and permeability determined for various paper grades and imaging techniques. Here, τ_{DX}, τ_{DY} and τ_{DZ} are the diffusive tortuosity values in the machine direction, cross direction and transverse direction, respectively, determined from the random walk simulations. Furthermore, given are the flow tortuosity τ_{FZ} and permeability k_{FZ} in the transverse direction, determined using direct numerical simulation by the lattice-Boltzmann method.

Sample	Image size	Resolution	τ_{DX}	τ_{DY}	τ_{DZ}	τ_{FZ}	k_{FZ}
Hand sheet	Small	High	2.69	3.47	16.0	3.78	0.0363
	Small	Low	1.21	1.36	2.93	1.98	0.343
	Large	Low	1.25	1.36	3.25	2.11	0.325
Newsprint	Small	High	1.43	3.50	6.76	2.32	0.117
	Small	Low	1.12	1.56	3.57	2.04	0.524
	Large	Low	1.07	1.36	2.96	2.24	0.548
Filter paper	Small	High	1.23	1.33	4.69	1.58	1.95
	Small	Low	1.16	1.23	1.99	1.52	1.62
	Large	Low	1.10	1.17	1.61	1.55	2.78

lower than that for the high-resolution images. The observed differences are most likely caused by the differences in the level of detail. It is clear from visual comparison that the high-resolution technique preserves the topology of the fibrous and porous structure better than the low-resolution technique.

Although the large-volume images are up to 34 times larger than the small-volume images, there are no significant differences between the respective characteristics. This indicates that even small volumes are sufficient for a good estimation of porosity and specific surface area.

4.1.3 Tortuosity and permeability

To gain a better understanding of the transport resistance of the samples, their tortuosities and permeabilities were measured, and the results are shown in Table 4.3. The largest differences between the tortuosities, in different paper grades as well as of different principal directions, were found in the high-resolution images, due to their higher level of detail. The smallest differences were found in the small, low-resolution images. Increased resolution will thus increase the differences in the measured tortuosity, and will thus improve the possibility to detect the effects of paper structure on the tortuosity and other transport properties. The low-resolution images will mostly provide correct trends in these properties, and are thus useful for comparative studies. Their applicability is limited by their lower ability to detect small particles such as fines, fillers and/or fibrils, and fibre-orientation anisotropy.

The flow tortuosity τ_{FZ} was found to be systematically lower than the diffu-

sive transverse tortuosity τ_{DZ}. This is expected since the streamlined hydrodynamic paths through the pore space are typically smoother than the winding random-walk paths of diffusive particles. However, the dependence of the flow tortuosity on various structural properties of the samples is qualitatively quite similar to that of the diffusive tortuosity, and the same qualitative analysis is valid for both. In the results for permeability and flow tortuosity, there is no significant difference between the values obtained for small and large samples (with low-resolution imaging). However, the permeabilities of the low-resolution images are systematically higher than those of the high-resolution images. The difference is moderate at high porosities but becomes significant at lower porosities. Obviously the poor resolution of the low-resolution images makes dense, complex structures more open for transport, while already open and relatively simple structures are affected less. In particular, the high-resolution results seem to be in qualitative agreement with the known limiting behaviour of flow tortuosity: it should approach unity as the porosity approaches unity, and diverge at some small but non-zero value of porosity (*i.e.* at the porosity corresponding to the percolation threshold). In general, results obtained for the high-resolution samples can be considered more reliable.

4.1.4 Reduced resolution and divided samples

Even though the results discussed above are qualitatively quite plausible, they are subject to uncertainty arising from the limited statistics available. In order to estimate the order of magnitude of purely numerical errors arising from the different discretizations used, we created a set of test samples by reducing the resolution of the original high-resolution images to that of the low-resolution images. The maximum difference between the tortuosities and permeabilities obtained for the original high-resolution samples and the reduced-resolution samples was about $20\ \%$.

The error due to the resolution should be compared against that due to sample size. The latter was estimated by dividing the original large images to several subimages, the size of which approximately coincided with that of the original smaller tomographic images. The maximum difference between the values calculated for the original large image and the mean value of the corresponding subimages was about $5\ \%$ for tortuosity and $20\ \%$ for permeability, and these values agreed very well with the Kozeny's law 2.13. We can thus conclude that numerical uncertainties are not very significant for the qualitative results obtained above. Instead, the natural variation intrinsic to paper material (the formation of paper) can be a much more important source of uncertainty for the results based on tomographic images. Based on the results for replicate tomographic samples and individual cropped subsamples, we estimate the uncertainty in the present results arising from the formation effect to be of the order of a factor two, both in the permeability and in the tortuosity.

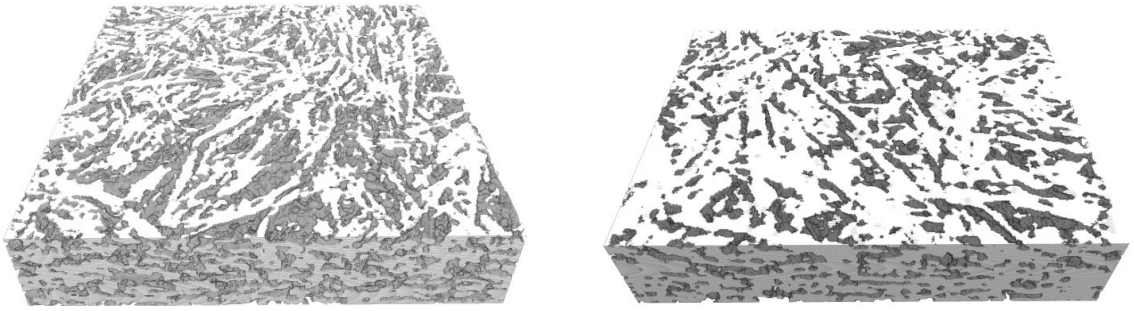

FIGURE 4.2 Tomographic images of paper samples CSF 670 (left) and CSF 460 (right).

4.2 Numerical analysis of fluid flow through tomographic images of paper

Hand sheets of a basis weight of $300\ \mathrm{g/m^2}$ were prepared from bleached softwood kraft pulp, that was beaten to different refining levels between 220 and 670 CSF in a laboratory beater. Three-dimensional $X - \mu CT$ images of the samples were made using the phase-contrast method [111, 112]. The resolution and the size of the images were about $2\ \mu\mathrm{m}$ and $1\ \mathrm{mm^2}$, respectively. Uneven paper surface layers were removed in the direction of the transverse (z) axis, whereby the thicknesses of the final samples varied between $120\ \mu\mathrm{m}$ and $200\ \mu\mathrm{m}$. Examples of structures generated by tomographic imaging of the paper samples are shown in Fig. 4.2.

The images of these samples were analyzed for the transverse and in-plane permeability, porosity, specific surface area, and tortuosity, using image-analysis techniques [32, 112] and lattice-Boltzmann flow simulations in these two orthogonal directions. Also, a reasonable comparison with conventional mercury-intrusion-porosimetry data from the same samples was obtained [32].

4.2.1 Lattice-Boltzmann and image-analysis results

In Fig. 4.3 we show the tortuosities given by the LB simulations and image analysis. The transverse and in-plane tortuosities were determined by LB flow simulations, and by image analysis that uses the chord-length distribution algorithm [32]. Interestingly, paper sheets formed as strictly layered structures in the laboratory sheet mold show little change in tortuosity with changing porosity (when the fibres were refined the density of the sheet was increased). However, the transverse tortuosity seems to undergo a significant change as a result of refining and densification, indicating a more complex, less permeable structure. Notice that the chord-length method tends to give higher values for tortuosity since the hydrodynamic tortuosity of Eq. (2.17) by the LB method gives more weight to paths of least resistance, whereas the chord-length method does not prefer any particular fluid path or chord length.

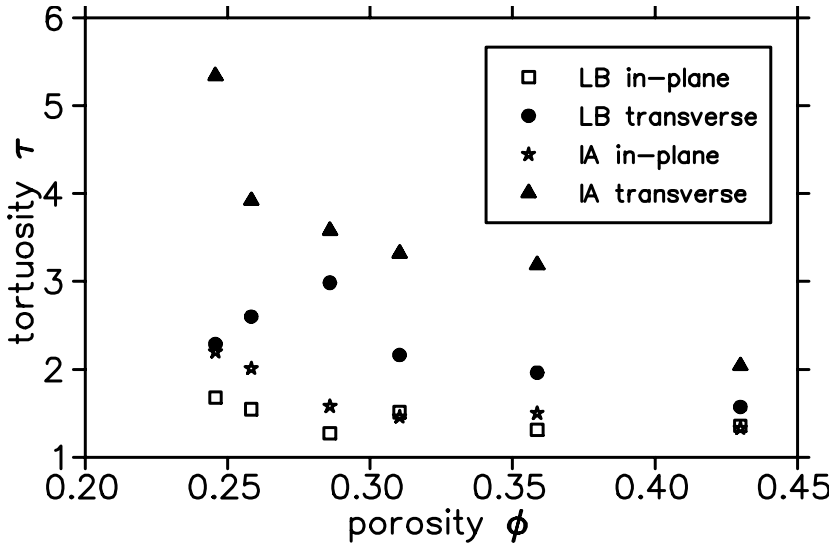

FIGURE 4.3 Transverse and in-plane tortuosities of paper samples given by LB simulations and image analysis.

In Fig. 4.4 we show the transverse and in-plane permeabilities of the paper samples. We compare the LB results with two fitting functions, the results of image-analysis techniques and some experiments [I, 116]. Darcy's permeability from Eq. (2.12) is determined directly by the LB method, whereas the image-analysis results are based on using the Kozeny law Eq. (2.13). The computed permeabilities of paper seem physically plausible, and, with the selected value of Kozeny's constant, $c = 2$, the results obtained from image analysis are quite close to those of LB simulations.

4.2.2 Experiments

For comparison, we also carried out experiments with the same paper grades as used in tomographic imaging. In this investigation, the in-plane water-flow characteristics of the paper samples were determined using a liquid/air displacement analyzer [I, 52] (see Sec. 2.3.4). Furthermore, the transverse air permeability of the CSF 670 sample was measured with the Polat method. Both lattice-Boltzmann and image-analysis results in Fig. 4.4 a) agree very well with the experimental value for this transverse air permeability. Comparing the computed and experimental values for the in-plane permeability shown in Fig. 4.4 b), a clear discrepancy can be seen. A plausible reason for this is that these experimental results were obtained using water, whereas dry samples were used in tomographic imaging. Due to swelling, the structure of the samples used in the experiments may not have been equivalent to those in the tomographic images. Another reason could be the limited resolution in tomographic imaging, which may be insufficient to resolve the complex microstructure of fibre surfaces. The specific surface obtained from the image analysis, and the

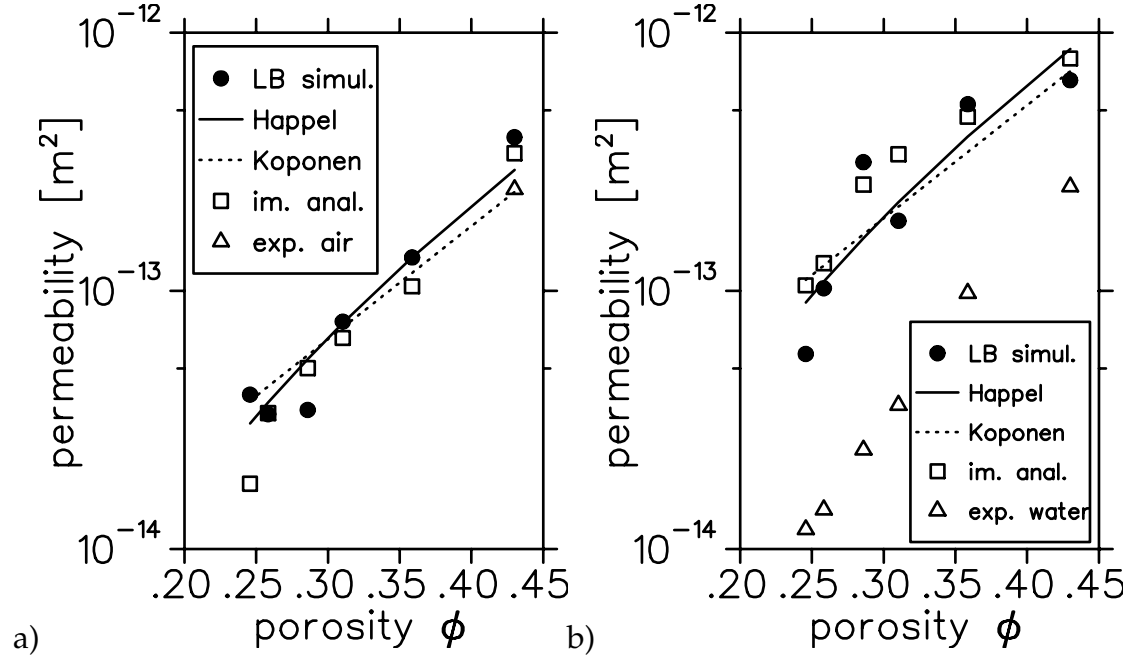

FIGURE 4.4 a) Transverse permeabilities of paper samples given by LB simulations, image analysis and one experimental point for air. b) In-plane permeabilities of paper samples given by LB simulations, image analysis and experimental values for water.

flow resistance given by the LB simulations, may be underestimated, which may have caused the computed permeability values to be above the experimental ones.

4.2.3 Fitting functions

The curves shown in Figs. 4.4 a) and b) are obtained by fitting two expressions using fibre radius a as the fitting parameter. The Happel formula Eq. (2.16) [39,40] is a theoretical construction for a regular array of rods, and the Koponen formula [I,89] is based on LB simulations and is proposed to explain the transverse permeability of PAKKA-model samples. They are relatively simple expressions and able to adequately describe the permeability of at least some materials, though not specifically that of real paper. The Kozeny equation Eq. (2.14) is not shown here, because its qualitative behaviour is very similar to that of Eq. (2.16), and the fitted curves would nearly overlap.

For the transverse permeability, Fig. 4.4 a), the fitted values of a are $5.05\ \mu\mathrm{m}$ and $2.25\ \mu\mathrm{m}$ for the Happel and Koponen formulae, respectively. For the in-plane permeability, Fig. 4.4 b), the corresponding values are $8.67\ \mu\mathrm{m}$ and $3.86\ \mu\mathrm{m}$. Both permeability formulae fit reasonably well the simulated results, but the Happel formula, Eq. (2.16), leads to a more realistic radius of the fibres, which can also be estimated from the images.

4.2.4 Quality review

The computed characteristic properties of paper seem physically convincing and the results obtained by different methods are consistent with each other. However, the absolute accuracy of the computed results for paper may still suffer from the quality of the tomographic imaging techniques used here.

As we saw in the comparison of the imaging techniques in Table 4.3, the permeabilities can be up to 10 times higher with the low resolution technique than with high-resolution technique. Resolution may also be a factor in the difference between the computed and experimental values in Fig. 4.4.

4.3 Fluid transport through woven fabrics

Polymeric carrier fabrics are commonly used in many industrial processes including manufacture of paper and board. The three-dimensional structure of the fabrics plays a critical role in deciding the manufacturing and energy efficiency of the process, as well as end-use properties of the product. Here, we used X-ray μCT to visualize the three-dimensional structure of polymeric fabrics commonly used in paper manufacture. 3D structural characteristics and fluid transport properties of the obtained tomographic images were measured with image-analysis techniques and the lattice-Boltzmann method.

4.3.1 Tomographic images

X-ray tomographic images were taken of two different types of paper-machine forming fabrics. Two samples of each wire type were imaged. We refer to these images/samples here by A1, A2, B1 and B2.

The resolution of the images was $4.41\ \mu\mathrm{m}$ and $4.34\ \mu\mathrm{m}$ for the A- and B-type samples, respectively. A typical yarn diameter was thus of the order of 40 pixels, so that the resolution of the images was very good, as for the level of discreteness effects. The lateral sizes of the rectangular images were about one unit cell of the wires, that were about $2.3 \times 2.2\ \mathrm{mm}^2$ and $3.0 \times 2.6\ \mathrm{mm}^2$ for the A- and B-type wires, respectively. Figure 4.5 shows the images of two of the wire samples.

Unlike disordered materials like paper, wires can be used to some extent to estimate the quality of the tomographic images used, as one can expect to obtain a regular interior structure. In this respect, one finds from the images that the surface of the wires seems somewhat 'rough', and spurious small solid obstacles seem to be created by the imaging procedure within the pore space. Correspondingly, the solid phase seems to contain incidental small voids. However, the error created by the small irregularities can be estimated to be very small - most likely of the order of a few per cent. We also tested the effect on simulation results of variations in

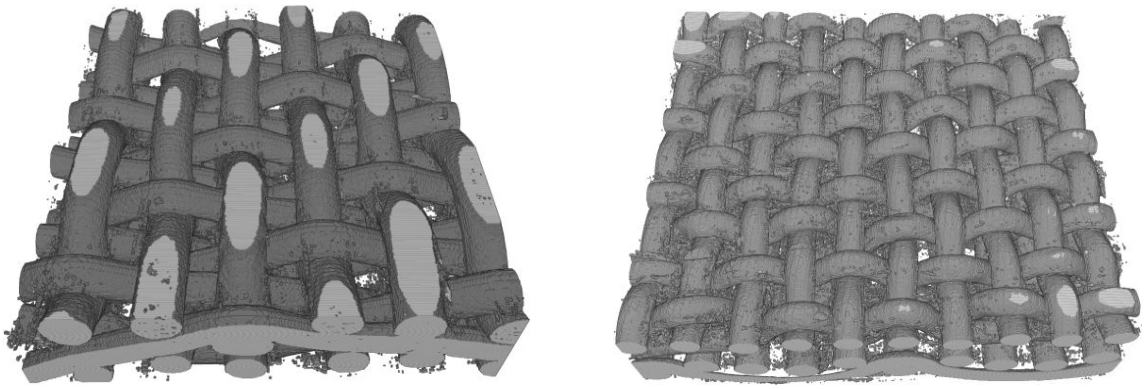

FIGURE 4.5 3D tomographic images of two types of wire samples, type A (left) and type B (right).

the boundary conditions and the viscosity of the fluid. All these effects were also found to be negligible as compared, e.g., to the difference between the two 'identical' samples for both wire types.

4.3.2 Lattice-Boltzmann results

Table 4.4 contains the simulated values for the four samples. Notice that these results are applicable only if flow rates are low, which is not always the case in the paper-making processes. For reference, given in the table is also the theoretical permeability derived by Happel (Eq. (2.16)) for fibrous porous media with high porosity. The pressure loss Δp across the wire of thickness T can be given optionally in terms of permeability k or pressure-loss coefficient K_0, such that

$$\Delta p = T\frac{\mu}{k}q = K_0\frac{\mu}{D}q, \tag{4.1}$$

where q is the flow velocity, μ is the dynamic viscosity of the fluid and D is the diameter of the yarn. The average radius a of the yarn is taken to be 0.08 mm for all the samples.

In general, the simulated porosities and permeabilities are higher for the B-type samples than for the A-type samples. In accordance with this, the simulated value for the pressure-loss coefficient is lower for the B-type samples. All the values simulated for the B1 and B2 samples are close to each other. Somewhat surprisingly, the values for thickness, porosity, permeability and pressure-loss coefficient differ significantly for the two A-type samples. The reason for this is that the tomographic image of the A2 sample, shown on left in Fig. 4.5, does not contain the entire wire in the thickness direction. This may also lead to differences in the permeability and the pressure-loss coefficient. The detected image of the A2 sample results from problems in tomographic imaging, but it actually corresponds to a worn wire in a paper machine. The permeability and pressure loss coefficient results suggest that water

TABLE 4.4 Structural parameters and Simulated quantities. The columns contain the following quantities: sample identifier, thickness (T), porosity (ϕ), Darcy permeability (k), theoretical permeability by Happel (k_{th}), pressure loss coefficient (K_0), specific surface (S, pore surface area/volume of the sample) and tortuosity (τ).

Sample	$T(\mathrm{mm})$	ϕ	$k(10^{-10}\mathrm{m}^2)$	$k_{th}(10^{-10}\mathrm{m}^2)$	K_0	$S(10^3/\mathrm{m})]$	τ
A1	0.66	0.530	0.937	2.0	2590	20.5	1.174
A2	0.58	0.479	0.510	1.2	1253	20.2	1.190
B1	0.87	0.526	1.47	3.5	1130	16.6	1.171
B2	0.87	0.560	1.61	4.0	1037	15.4	1.166

removal is impaired when the wire is worn. The theoretical values based on the Happel formula Eq. (2.16) are systematically higher than, but nevertheless of the same order of magnitude as the simulated values. This is as expected since the theoretical result is based on independent fibres and may be considered as a theoretical upper bound for real fibrous porous media.

Another error source evident in the images is that the samples used in the imaging have obviously been too small so that the images do not always contain an entire waving unit. Periodicity is thus not complete. The edges of the samples seem to contain some irregularities, which may have been created by cutting the samples for imaging. Cutting may have affected the contacts between wires and the overall density of the wire near the edges.

Comparison of the average yarn diameters as produced by $X - \mu CT$ together with image analysis and a direct measurement using light microscopy, agreed to within $3\ \%$, indicating good accuracy of the X-ray technique [III].

4.4 Fluid flow through PAKKA-model structures

Within the numerical PAKKA model (see Sec. 3.8) [102,107], fibre webs are grown by randomly depositing flexible fibres of rectangular cross section on a flat substrate. These webs are periodic in the in-plane (x and y) directions. In order to make the structures homogeneous, surface layers perpendicular to the z axis were removed. The porosity of the samples is controlled by varying the flexibility of the deposited fibres. In the earliest version of the model, fibres were randomly oriented in two perpendicular directions. The fibre width to length ratio used here was 1:20, and the size of the samples was four fibre lengths in the x and y directions and ten fibre widths in the z direction. Later versions of the model include random orientation, flattened fibres, and fines. Examples of structures generated by the model are shown in Fig. 4.6.

The structures were discretized for the lattice-Boltzmann simulations based on

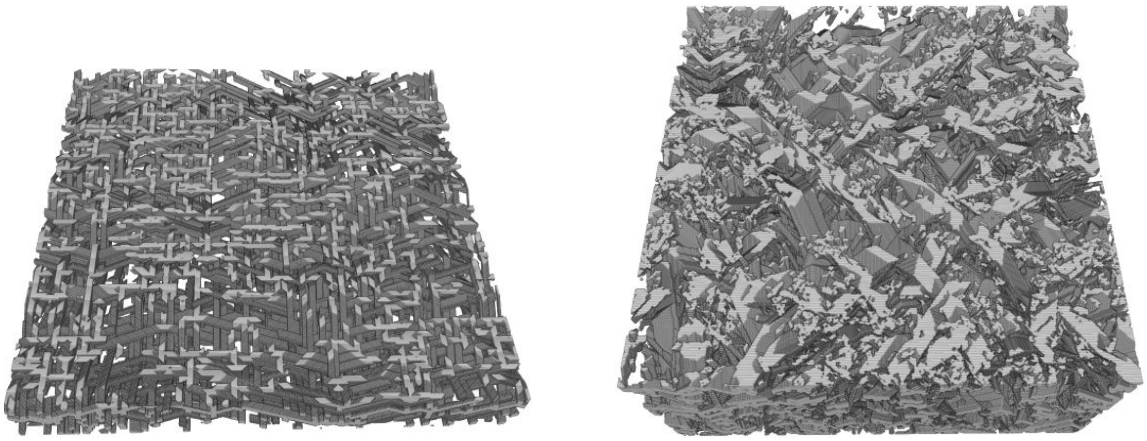

FIGURE 4.6 PAKKA-model samples: A sample with fibres oriented in two perpendicular directions (left) and a sample with fines and randomly oriented fibres (right).

previous rigorous studies [89] of discretization effects (see Sec. 3.7.4) in samples of different porosities. The final structures used in the simulations were constructed with fibre widths of 5, 10 and 20 lattice units, so that the low-porosity samples had the finest discretization.

4.4.1 Transverse and in-plane fluid flow

Lattice-Boltzmann simulations were done for Stokesian fluid flow through samples of the earliest version (on the left in Fig. 4.6) of the PAKKA model. Simulations were carried out both in the in-plane and transverse directions to determine the anisotropy of permeability, which is an important quantity in many processes such as wet pressing.

The boundary conditions imposed in the simulations were selected so as to utilize the structural symmetry inherent in the model and to minimize the effects of the finite size of the samples. In the transverse-flow simulations, free fluid layers of at least 10 % of the thickness of the sample were added above and below the sample, and periodic boundary conditions were imposed in the z direction. Periodic boundary conditions were imposed also in the x and y directions as the PAKKA model structures are periodic in these lateral directions. For the in-plane flow simulations the frictionless slip condition was used at the boundaries perpendicular to the z direction, corresponding to reflection symmetry across these boundaries (to minimize the finite-size effects). The numerical accuracy of the flow-simulation results was dominated by discretization effects, and they were estimated with multiplied grids (see Sec. 3.7.4) to be less than 15 % for the simulated permeability values.

In Fig. 4.7 a) we show the simulated transverse [I, 89] and in-plane [I] permeabilities of the PAKKA samples together with various experimental results for the transverse permeability of different materials made of artificial and natural fibres [39]. The simulated values are seen to agree very well with the experimen-

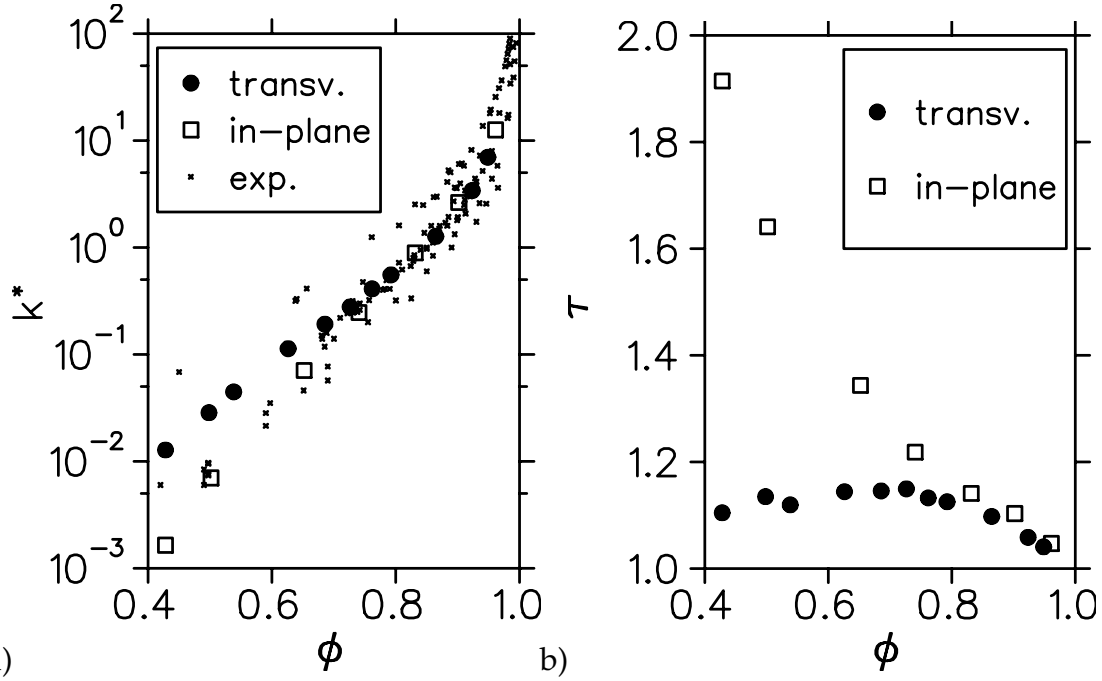

FIGURE 4.7 a) Transverse and in-plane dimensionless permeability $k^* = k/a^2$ vs. porosity ϕ for PAKKA-model samples. Here, a is the hydraulic radius of the rectangular fibres. The experimental data is for transverse permeability of various fibrous filters [39]. b) Transverse and in-plane tortuosity τ vs. porosity ϕ for PAKKA-model samples.

tal ones in a broad range of porosity. We also see that the in-plane and transverse permeabilities of the PAKKA samples are approximately equal down to $\phi \approx 0.6$, whereas for low porosities the in-plane permeabilities are significantly smaller. This is contrary to our simulation results for the paper samples (Sec. 4.2) and to earlier experimental results for paper [108, 117]. The reason for this behaviour is the rectangular cross-sectional shape and the fibre-bending mechanism used in the PAKKA model. For high values of the bending parameter (which leads to low-porosity structures) the fibres become strongly bended in the z direction. As a consequence, fibres disperse the fluid flow much more efficiently in the transverse direction making the pathlines more tortuous in the in-plane directions. In Fig. 4.7 b) we show the simulated transverse and in-plane tortuosities. The difference between the transverse and in-plane permeabilities was indeed found to result mostly of the assumed $k \propto 1/\tau^2$-behaviour of permeability in Eq. (2.13), *i.e.*, substitution of the values of permeability, porosity, pore surface area and tortuosity in Eq. (2.13) gave relatively small variation in the Kozeny's constants c thus obtained.

At high porosities the tortuosity effects are not dominant, and according to the theoretical results given *e.g.* in Ref. [39], the ratio of permeabilities of cylindrical rods perpendicular and parallel to the flow is $1 : 2$. In the PAKKA model, all fibres are perpendicular to the flow in the transverse-flow simulations, whereas half of the

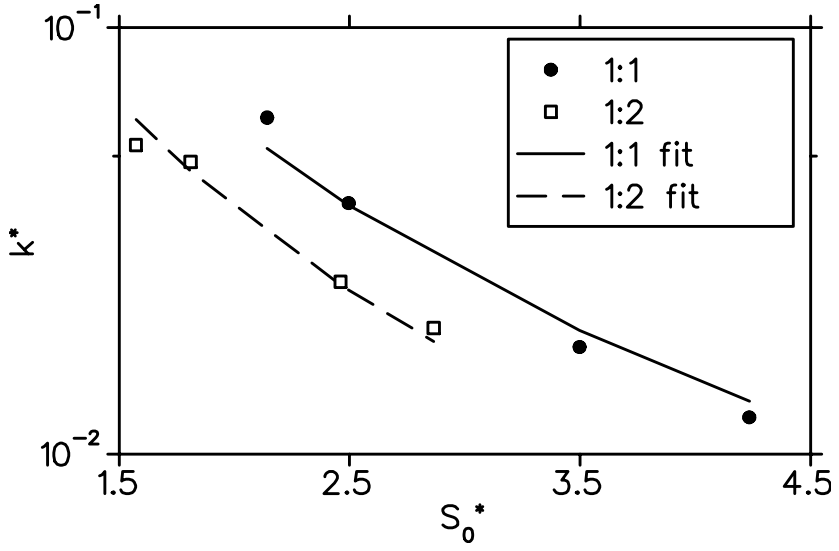

FIGURE 4.8 The dimensionless transverse permeability $k^* = k/a^2$ vs. dimensionless specific surface area $S_0^* = S_0 a$ at a constant porosity $\phi = 0.60$ for fibres with cross-sectional height to width ratios of $1:1$ and $1:2$. Here, a is the hydraulic radius of the rectangular fibres. For both shapes of fibres, the four points shown correspond to relative fines contents of 0, 10, 30 and 50 % (increasing with increasing S_0^*). Also shown are fitted curves with $k \propto 1/S_0^2$.

fibres are perpendicular and half parallel to the flow in the in-plane simulations. At high porosities, the value of the in-plane permeability given by our simulations is about 1.5 times that of the transverse permeability, which is very much as expected. This small difference is not clearly visible in Fig. 4.7 a) due to the logarithmic scale.

4.4.2 Effect of flattened fibres and the fines content

In paper, fibres may be flat and contain fibrils, and the solid phase includes varying amounts of fines and fillers. In order to study the qualitative effect of these properties on transverse permeability, samples of the later version (on right in Fig. 4.6) of the PAKKA model were created with fibres of square cross section, and with fibres of flat rectangular cross section (height to width ratios of $1:1$ and $1:2$, respectively). Furthermore, small cubic particles with the side length $1/4$ of the width of the fibres were randomly deposited on fibre surfaces. The amount of these 'fines' particles varied from 0 to 50 % of the total solid volume fraction which was kept close to a constant value $\varphi = 0.40$. The transverse LB fluid flow simulations were done, and all the permeabilities were adjusted with the Kozeny law Eq. (2.14) to correspond to the porosity value $\phi = 0.60$. The resulting dimensionless permeabilities, scaled with the hydraulic radii of the square-shape and flattened fibres, are shown in Fig. 4.8 [V, I]. The flatteness of the fibres decreases the permeabilities of the fibre webs. Moreover, the permeability decreases rapidly with increasing fines content, and this

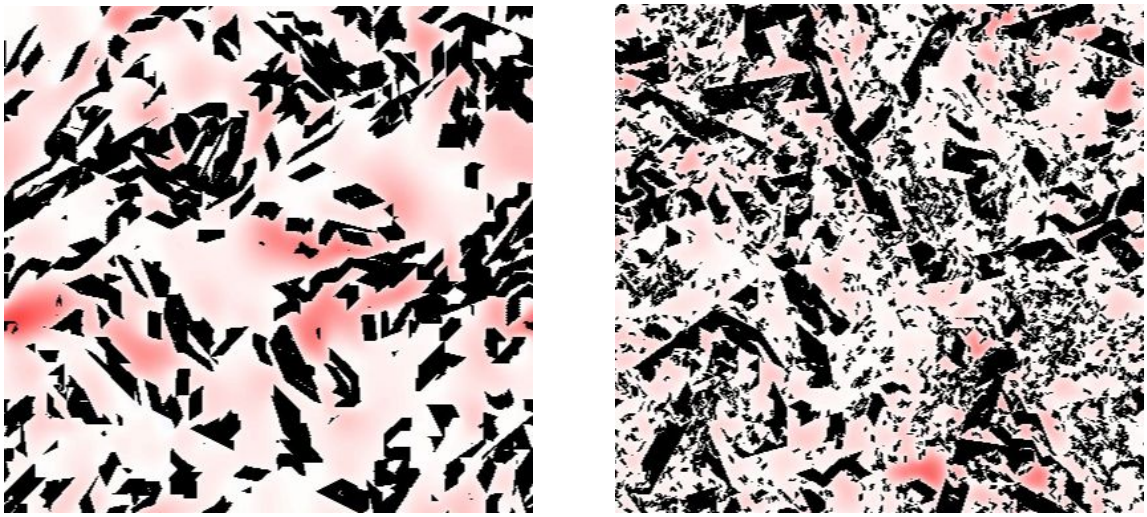

FIGURE 4.9 2D horizontal sections in the middle of the simulated flow fields in PAKKA samples of 0 % (left) and 50 % (right) of fines content. Black colour indicates solid area, and white and dark colours in the pore area indicate low and high velocities, respectively.

behaviour is very well explained by its dependence on the specific surface area, as given by the Kozeny equation, namely $k \propto 1/S_0^2$.

4.4.3 Local variation of flow field

There are many ways to consider local variations of the flow field in a sample, and one approach is to divide the sample into smaller parts [4], and then to simulate fluid flow separately in each part [IV, 118]. A slightly different approach would be to use the flow field of the whole sample and to consider the local variations of flow and structural characteristics in it. We adopt here the latter approach.

In these simulations the force is applied in the z (thickness) direction, and local variations in the flow field are considered in the xy plane. The x- and y-boundary effects are not present since the PAKKA samples are periodic. We present results for the finest possible division of the sample into discrete local units in which the dimensions of the local units are one lattice spacing in the x and y directions, while having the thickness of the sample in the z direction. We study in particular the relation between some structural characteristics of the sample and the local transverse flux that is related to local permeability. In Fig. 4.9 we show two cross sections perpendicular to main flow of simulated velocity fields in PAKKA samples of 0 % and 50 % of fines content. Fines tend to disperse the flow field more efficiently than mere fibres.

For the analysis, the flux is divided into ten classes by its magnitude, and the structural characteristics considered are averaged separately over the units that are in each flux class. In Fig. 4.10 shown are four network characteristics as a function

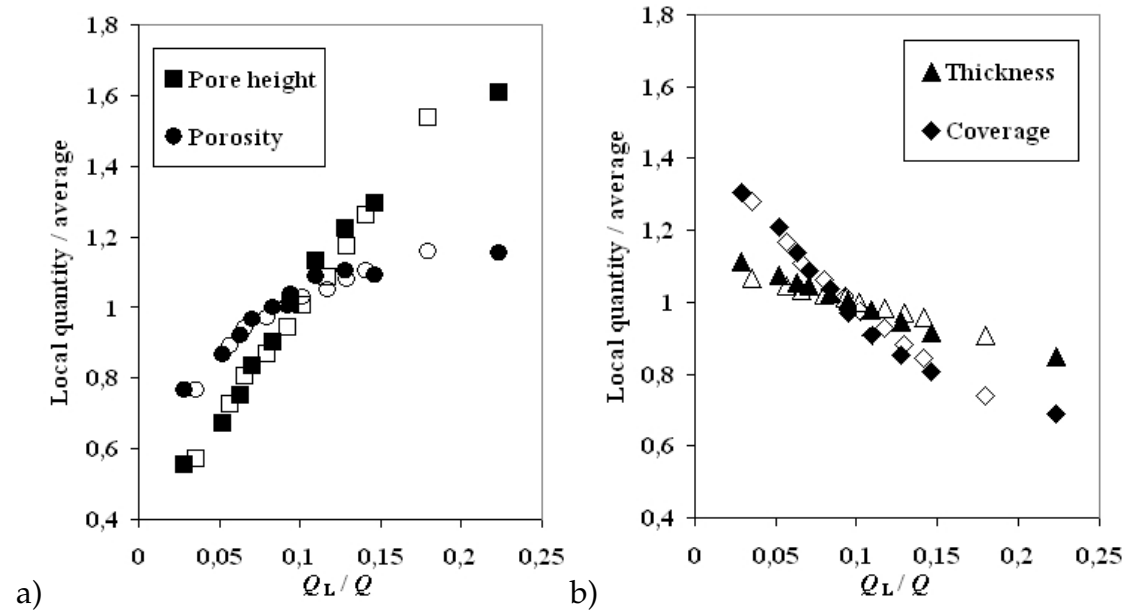

FIGURE 4.10 a) Relative pore height and porosity, and b) thickness and coverage as a function of local flux Q_L/Q for PAKKA-model samples. The results are shown for the samples of 0 % (filled markers) and 50 % (open markers) of fines content.

of flux. Results are shown for samples that have 0 % and 50 % fines content. The values for the other concentrations lay between the shown ones. Each characteristics is divided by its average value for the whole sample, the flux values are divided by the total flux.

In Fig. 4.10 a) shown are the pore height, *i.e.* the average height of unbroken void space, and porosity. As expected, both these quantities increase with increasing flux. The increase in porosity is clearly non-linear, in accordance with the typical dependence of permeability on porosity (see Sec. 2.3.2). The latter dependence is approximately logarithmic in this porosity range [89]. In Fig. 4.10 b) shown are the thickness, *i.e.* the distance between the first and last solid points in the z direction, and the coverage, *i.e.* the solid fraction of the thickness. These quantities decrease, as one can expect, with increasing flux. Clearly higher local flux values are found in the case of no fines particles. This is also expected since in this case larger and less tortuous pores through the sample can appear.

The large differences between the highest flux values in the division into ten equal-sized classes is related to the shape of fluid-speed distribution which, in this case of PAKKA-model samples, is very similar to that formed to Fontainebleau sandstone (cf. Fig. 4.13). Division of the fluid-speed distribution into ten classes of equal size would result in a similar difference between the classes of highest speeds. The differences between flux classes in Fig. 4.10 are most pronounced for the sample without fines, which indicates that flow is in this case channelled more through a few largest pores than in samples that include fines.

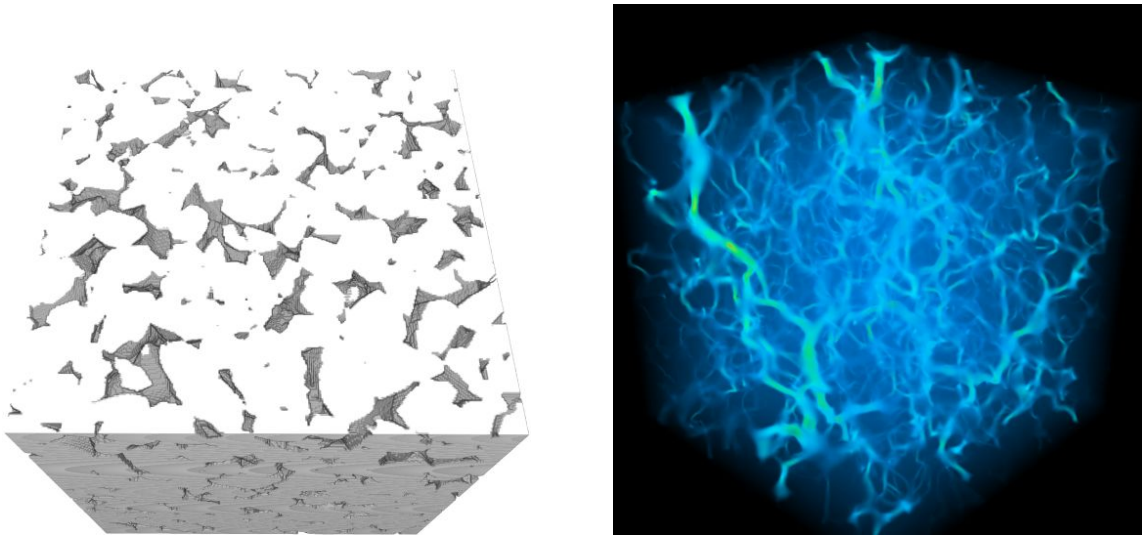

FIGURE 4.11 Tomographic image of Fontainebleau sandstone (left) and fluid flow (right) in the pore space simulated with the lattice-Boltzmann method. Light and dark colours indicate high and low velocity, respectively.

4.5 Fluid flow in sandstone models

We simulated, with the lattice-Boltzmann method and the finite-difference method [II], the permeability of a tomographic image of a sample of Fontainebleau sandstone, and of three different constructions of this sample based on its correlation properties. The linear size of the sample was approximately 3 mm, and the image resolution was 7.5 μm. The accuracies of the two methods are discussed and the results are compared also with experiment.

4.5.1 Samples

Fontainebleau sandstone is a popular reference standard because of its exceptional chemical, crystallographic and microstructural simplicity [119, 120]. Intergranular porosity of this sandstone ranges from 0.03 to roughly 0.3 [120]. A computed microtomographic image was taken of a micro-plug from a larger original core of porosity $\phi^* = 0.1484$ and permeability $k^* = 1.3$ D (1 D=0.987 μm^2). The microtomographic image had the dimension $299 \times 300 \times 300$ voxels, and a porosity of $\phi = 0.1355$. In the following we denote by EX this microtomographic image of Fontainebleau sandstone. In Fig. 4.11 we show the visualizations of the sample EX and the flow field through it.

The three constructed samples are physical and stochastic reconstruction models for sample EX. All have the same lattice resolution, $a = 7.5$ μm, and approximately the same porosity and specific surface area. The diagenesis model (DM) [103] is a physical model that mimics the processes of sedimentation, compaction and diagenesis of sandstone. The DM sample had the dimension $255 \times 255 \times 255$ voxels.

TABLE 4.5 Geometrical characteristics of the four samples: ϕ is the porosity, S_V the specific surface area, f_p the fraction of percolating pore lattice points and $p_3(60a)$ ($a =$ lattice spacing) the probability of finding a cubic subblock of size $L = 60a$ of the sample, which is percolating in all three directions.

	EX	DM	GF	SA
ϕ	0.1355	0.1356	0.1421	0.1354
$S_V\ [mm^{-1}]$	9.99	10.30	14.53	11.04
f_p [%]	99.35	99.23	79.16	62.73
$p_3(60a)$	0.9561	0.9647	0.3255	0.1695

The simulated-annealing (SA) and gaussian-field (GF) samples were stochastic reconstructions [31,103,106] for sample EX with the dimension $256 \times 256 \times 256$ voxels. They had about the same porosity, specific surface area and two-point correlation function as the Fontainebleau sample. In Table 4.5 we give some geometrical characteristics of the samples. The models for DM and SA are introduced in Sec. 3.8.1 and the samples are shown in Fig. 3.7.

4.5.2 Permeability

We applied BGK lattice-Boltzmann (LB) and finite-difference (FD) algorithms [II] to the solution of Stokes flow through the experimental sample EX and the model samples DM, GF, and SA. In Table 4.6 are given the components of the permeability tensors for all four samples and for both algorithms. The diagonal elements describe the flow resistance in the applied force directions, and the other elements are due to sideflows that are expected to become nebligible if the samples were isotropic and large.

The permeabilities are strongly correlated with the geometrical connectivity of the pore space, as measured by the total fraction of percolating cells $p_3(L)$. We find that the permeability of the original sandstone EX and that of the process model DM are in good agreement, while the permeabilities of the stochastic models GF and SA are an order of magnitude smaller. It seems as if the stochastic reconstruction models cannot reproduce the high degree of geometrical connectivity present in the original sandstone. The reconstructed two-point correlation function lacks information about the geometrical connectivity of the pore space. A correct description of the geometrical connectivity is however important for reliable transport properties. The permeability results confirm the predictions from a previous purely geometrical analysis based on local porosity theory [103], in which the importance of local connectivity is emphasized.

TABLE 4.6 Permeability tensors of the Fontainebleau sandstone and its models. The values are given in mD (1 D=0.987 μm^2).

	FD			LB		
	k_{i1}	k_{i2}	k_{i3}	k_{i1}	k_{i2}	k_{i3}
EX	692	47	−15	621	40	−15
	15	911	50	14	808	47
	−103	21	789	−85	15	687
DM	923	40	16	766	31	10
	27	581	25	19	482	22
	21	35	623	14	32	528
GF	34	1	4	43	3	6
	0	35	2	1	50	6
	8	1	36	7	4	57
SA	35	0	5	56	−2	7
	−7	22	−1	−5	46	13
	3	−7	20	8	1	50

4.5.3 Comparison with experiment

We compared the numerically obtained value of the permeability k_{EX} of sample EX with the experimental value $k^* = 1.3$ D, which requires a correction due to the difference between the porosity of the EX sample and the porosity $\phi^* = 0.1484$ of the original core sample. To this end we used an experimental correlation between porosity and permeability [II, 120],

$$k = A\phi^b, \tag{4.2}$$

in which A and b are constants. In the porosity range of interest, $\phi \approx 0.13 - 0.15$, this correlation has $b \approx 4$, with however a large uncertainty due to scatter in the measured results. Hence, we can extrapolate the numerically determined permeabilities $\bar{k} = (k_{11} + k_{22} + k_{33})/3$ into the prediction

$$\bar{k}^* = \bar{k} \left(\frac{\phi^*}{\phi} \right)^b, \tag{4.3}$$

where ϕ^* is the previously defined porosity of the core sample. From Eq. (4.3) we obtain $\bar{k}^* = 1150$ mD for the FD method and $\bar{k}^* = 1015$ mD for the LB algorithm. These values are quite close to the experimental value $k^* = 1300$ mD.

4.5.4 Comparison of the methods

An accurate, quantitative comparison of the two numerical methods is difficult due to the different approaches underlying these methods. The memory requirements of

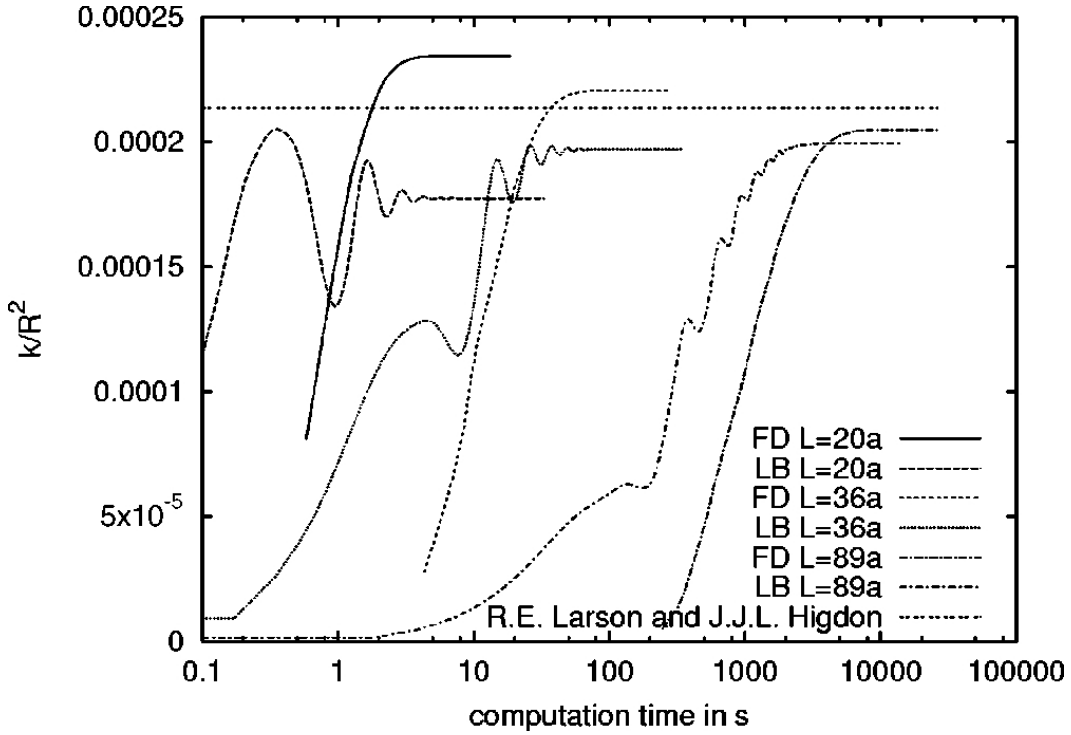

FIGURE 4.12 Time evolution of the numerical solution of the permeability k for flow through a cubic array of spheres with porosity $\phi = 0.15$. The relaxation parameter was $\xi = 0.688$ for the LB simulations. The horizontal line gives the reference value k_{ref}.

the algorithms used in this study differ by roughly a factor of 4. The FD algorithm requires to store 5 real numbers per lattice node, while the LB algorithm used needs 19 real numbers per node.

To test the efficiency of these two algorithms we used the same samples of cubic arrays of spheres as in Sec. 3.7.2. In Fig. 4.12 [II] we compare the time evolution of the numerical value of the permeability k for different system sizes. Plotted on the x axis is the total time in seconds needed on two processors. For $L = 20a$ and $L = 36a$, both methods reach the final value of k in approximately the same time. For large L the LB method seems to be faster. Notice that the results of the LB simulations shown in Fig. 4.12 were performed for $\xi = 0.688$. As given by the Eq. (3.52), higher $\nu \propto \xi$ gives smaller saturation time, and for $\xi = 1.0$ the simulations were about 45 % faster.

The convergence of $k(t)$ towards its asymptotic value is monotonic for the FD method, while in the LB case $k(t)$ shows oscillations for all L. The reason for these oscillations is probably the slight compressibility error inherent in the model [8,9]. The horizontal line in Fig. 4.12 gives the reference value k_{ref} towards which the asymptotic values of both algorithms converge with L.

Figure 4.13 [II] shows the scaled distributions of the magnitude of the fluid velocity $|\vec{v}|$ for samples EX and SA. The higher permeability of the original sandstone

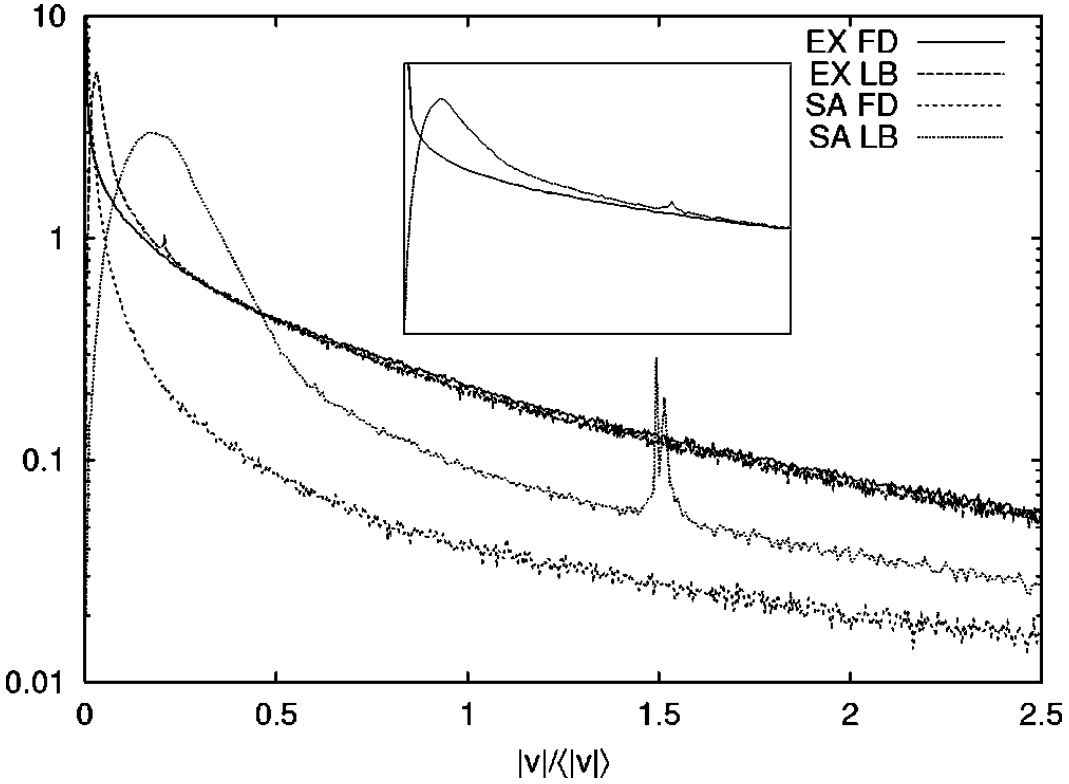

FIGURE 4.13 Velocity distribution function $P(|\vec{v}|)$ of the Fontainebleau sandstone (EX) and the SA model sampled over the pore space. The distributions are scaled with the mean velocity $\langle|\vec{v}|\rangle$. The inset shows a magnification of the distribution of EX for small velocities.

EX is reflected by a higher probability density of regions with average flow velocity. The distribution of sample SA on the other hand exhibits a higher peak at $|\vec{v}| = 0$, and it extends to higher velocities. The former observation indicates large stagnant areas where no transport is taking place. The increased probability at high velocities may be related to a large number of narrow pore throats through which the fluid has to move. The velocity results for sample GF resemble closely to those of sample SA while those for sample DM resemble those for EX.

The distributions obtained from the LB solution exhibit a maximum at small velocities which is not present in the distributions obtained from the FD solution. The differences could perhaps be attributed to the slip velocities due, *e.g.*, to the bounce-back boundary condition and the diagonal leak flows in the LB algorithm, which could lead to a systematic deficit of zero velocities near the boundary.

For SA there is an additional spurious peak at $|\vec{v}|/\langle|\vec{v}|\rangle \approx 1.5$. Similar, although smaller peaks were also found for GF and EX. The locations of these peaks were found to be $\Delta p/2\rho\langle|\vec{v}|\rangle$, where Δp is the body force. We attribute these peaks to the staggered momenta found in small closed pores, the number of which is very high for SA and GF. The spurious peaks could have been eliminated by time averaging

the velocities.

As discussed earlier, there are some features in the standard application of the LB method, which need special attention. In this comparison the most significant ones are the finite-size effect coupled to the ξ dependence of the no-slip boundary, and diagonal leak flows (see Sec. 3.5). The latter becomes noticeable for rough surfaces especially near the percolation threshold, and limit only there the accuracy of the method. If needed, they can also be eliminated by fairly straightforward means, applying the bounce-back on the leaking links.

Chapter 5

Conclusions

We used the lattice-Boltzmann method to solve 3D Newtonian fluid-flow problems in porous media obtained by tomographic imaging and by numerical modelling. By lattice-Boltzmann simulations we examined the quality of numerical models of porous media and present-day tomographic imaging techniques. Models were found to give a qualitatively plausible dependence of permeability on porosity, but also effects of other structural properties were demonstrated. These involve specific surface area, tortuosity, and shape and orientation of particles in the medium. Generally, all the simulated permeabilities were consistent, and in each case they complied with well-known formulae such as the Kozeny law. Deviations from the Kozeny law were well explained by the determined tortuosities and specific surface areas.

We found that tomographic imaging is capable of producing representative structures of sandstone, woven fabrics and many paper grades. Transverse and in-plane flow simulations in paper images and PAKKA-model samples augmented the characteristics of the samples and revealed *e.g.* the effect of fibre flexibility. Furthermore, the simulations show that results on paper can be sensitive to imaging techniques, since the permeability differences between low- and high-resolution images can be noticeable, though the results within each technique were consistent. Our results also show that fluid-flow simulations for PAKKA-model samples and tomographic images of some paper grades, can produce results that are similar to those found in experiments. There are obviously also experimental factors, such as *e.g.* swelling of fibres in water, which are not included in the present simulations. The fluid flow simulation results of various paper grades could increase the reliability of modelling the paper-making processes, and those of wires the possibilities to examine and develope the paper-machine clothing.

Our simulations of fluid flow through sandstone models show that a tomographic image of sandstone, and to some extent also the physical diagenesis model, reproduce the experimental permeability of the real sandstone quite accurately, while the permeabilities of the stochastic reconstructions deviate from the latter by at least

an order of magnitude. We demonstrated also that the performances of the lattice-Boltzmann method and conventional finite-difference method are quite similar in terms of accuracy and computational resources when solving the Stokes equation.

The rapidly developing lattice-Boltzmann method is a flexible and convenient tool. As we have demonstrated here, one of the successful applications of the method is simulating fluid flow in porous media. Among its benefits are the simplicity of a uniform grid and of realizing the no-slip boundary condition by the bounce-back rule. These features are advantageous for fluid-flow problems in complex geometries. The LB method is also well suited for parallel computing because of the spatial locality of the updating rules. In many cases of flow in porous media, even the simplest realization of the LB method can be used to obtain quantitatively good results.

A shortcoming of the LB method is the difficulty, as also in other numerical methods, to simulate flows at high Reynolds numbers. In practical applications very large computational lattices are also required, which means that high-performance computing is needed. Continuously developing computing power improves the situation, but compromises between system size and resolution will still be needed. Improving resolution of tomographic images into the sub-micrometer regime means that system sizes tend to stay more or less constant while the number of voxels they contain is increased.

In conclusion, the large-scale simulations with realistic images of porous materials carried out in this work, have indeed given us new insight into the classic problem of the dependence of permeability on other macroscopic characteristics of the material. Obviously unsolved problems still remain, but the approach chosen here to this problem has proved to be very promising.

Bibliography

[I] U. Aaltosalmi, M. Kataja, A. Koponen, J. Timonen, A. Goel, G. Lee, S. Ramaswamy, Numerical analysis of fluid flow through fibrous porous materials (2004).

[II] C. Manwart, U. Aaltosalmi, A. Koponen, R. Hilfer, J. Timonen, Lattice-Boltzmann and finite difference simulations for the permeability of three-dimensional porous media (2002).

[III] S. Ramaswamy, M. Gupta, A. Goel, U. Aaltosalmi, M. Kataja, A. Koponen, B. V. Ramarao, Efficient simulation of flow and transport in porous media (2004).

[IV] R. Holmstad, U. Aaltosalmi, S. Ramaswamy, M. Kataja, A. Koponen, A. Goel, Ø. W. Gregersen, Comparison of 3D structural characteristics of high and low resolution X-ray microtomographic images of paper (2004).

[V] M. Rasi, A. Koponen, U. Aaltosalmi, J. Timonen, M. Kataja, K. J. Niskanen, Permeability of paper: Experiments and numerical simulations (1999).

[1] M. Sahimi, Flow and Transport in Porous Media and Fractured Rock, VCH, Weinheim, 1995.

[2] H. Darcy, Les Fontaines Publiques da la Ville de Dijon, Dalmont, Paris, 1856.

[3] A. Scheidegger, The physics of flow through porous media, Macmillan, New York, 1957.

[4] J. Bear, Dynamics of Fluids in Porous Media, Dover, New York, 1972.

[5] P. Knupp, S. Steinberg, Fundamentals of Grid Generation, CRC Press , Boca Raton, FL, 1993.

[6] Y. H. Qian, D. d'Humiéres, P. Lallemand, Lattice-BGK models for Navier-Stokes equation, Europhys. Lett. 17 (6) (1992) 479–484.

[7] R. Benzi, S. Succi, M. Vergassola, The lattice-Boltzmann equation: theory and application, Phys. Rep. 222 (3) (1992) 145–197.

[8] D. H. Rothman, S. Zaleski, Lattice-Gas Cellular Automata: Simple Models of Complex Hydrodynamics, Collection Aléa, Cambridge University Press, Cambridge, 1997.

[9] B. Chopard, M. Droz, Cellular automata modelling of physical systems, Cambridge University Press, Cambridge, 1998.

[10] S. Chen, G. D. Doolen, Lattice Boltzmann method for fluid flows, Annu. Rev. Fluid Mech. 30 (1998) 329–364.

[11] S. Succi, The lattice Boltzmann Equation for Fluid Dynamics and Beyond, Oxford University Press, Oxford, 2001.

[12] X. He, L.-S. Luo, A priori derivation of the lattice Boltzmann equation, Phys. Rev. E 55 (1997) R6333–R6336.

[13] U. Frisch, D. d'Humiéres, B. Hasslacher, P. Lallemand, Y. Pomeau, J.-P. Rivet, Lattice gas hydrodynamics in two and three dimension, Complex Syst. 1 (1987) 649–707.

[14] D. H. Rothman, S. Zaleski, Lattice-gas models of phase separation: interface, phase transition and multiphase flows, Rev. Mod. Phys. 66 (1994) 1417–1479.

[15] U. Frisch, B. Hasslacher, Y. Pomeau, Lattice-gas automata for the Navier-Stokes equation, Phys. Rev. Lett. 56 (1986) 1505–1508.

[16] D. d'Humiéres, M. Bouzidi, P. Lallemand, Thirteen-velocity three-dimensional lattice Boltzmann model, Phys. Rev. E 63 (2001) 066702.

[17] G. McNamara, G. Zanetti, Use of the Boltzmann equation to simulate lattice-gas automata, Phys. Rev. Lett. 61 (1988) 2332–2335.

[18] F. Higuera, J. Jimenez, Boltzmann approach to lattice gas simulations, Europhys. Lett. 9 (7) (1989) 663–668.

[19] F. Higuera, S. Succi, R. Benzi, Lattice gas dynamics with enhanced collision, Europhys. Lett. 9 (4) (1989) 345–349.

[20] D. d'Humiéres, Generalized lattice-Boltzmann equations, in: B. D. Shizgal, D. Weaver (Eds.), Rarefied gas Dynamics: Theory and Simulations, Vol. 159, Progress in Astronautics and Aeronautics, 1992, pp. 450–458.

[21] P. Lallemand, L.-S. Luo, Theory of the lattice Boltzmann method: Dispersion, dissipation, isotropy, Galilean invariance, and stability, Phys. Rev. E 61 (2000) 6546–6562.

[22] D. d'Humiéres, I. Ginzburg, M. Krafczyk, P. Lallemand, L.-S. Luo, Multiple-relaxation-time lattice Boltzmann models in three dimensions, Phil. Trans. R. Soc. Lond. A 360 (2002) 437–451.

[23] K. Balasubramanian, F. Hayot, W. F. Saam, Darcy's law from lattice-gas hydrodynamics, Phys. Rev. A 36 (5) (1987) 2248–2253.

[24] D. H. Rothman, Cellular automaton fluids: a model for flow in porous media, Geophys. 53 (1988) 509–518.

[25] S. Succi, E. Foti, F. Higuera, Simulation of three-dimensional flows in porous media with the lattice Boltzmann method, Europhys. Lett. 10 (5) (1989) 433–438.

[26] A. Cancelliere, C. Chang, E. Foti, D. Rothman, S. Succi, The permeability of a ramdom medium: Comparison of simulation with theory, Phys. Fluids A 2 (12) (1990) 2085–2088.

[27] S. Chen, K. Diemer, G. Doolen, K. Eggert, C. Fu, S. Gutman, B. Travis, Lattice gas automata for flow through porous media, Physica D 47 (1991) 72–84.

[28] B. Ferréol, D. H. Rothman, Lattice-Boltzmann simulations of flow through fontainebleau sandstone, Transport in Porous Media 20 (1–2) (1995) 3–20.

[29] A. J. C. Ladd, Numerical simulation of particulate suspensions via a discretized Boltzmann equation, J. Fluid Mech. 271 (1994) 285–309.

[30] C. Aidun, Y. Lu, Lattice Boltzmann simulation of solid particles suspended in a fluid, J. Stat. Phys. 81 (1995) 49–59.

[31] S. Torquato, Random Heterogeneous Materials, Springer Verlag, New York, 2001.

[32] S. Ramaswamy, S. Huang, A. Goel, A. Cooper, D. Choi, A. Bandyobadhyay, B. V. Ramarao, The 3D structure of paper and its relationship to moisture transport in liquid and vapor forms, in: The Science of Papermaking - Trans. 12th Fundamental Research Symposium, Vol. 2, The Pulp and Paper Fundamental Research Society, Bury, Lancashire, UK, 2001, pp. 1281–1311.

[33] F. M. White, Fluid Mechanics, McGraw-Hill, New York, 1994.

[34] P. M. Chaikin, T. C. Lubensky, Principles of condensed matter physics, Cambridge University Press, Cambridge, 1995.

[35] R. Fox, A. McDonald, Introduction to fluid mechanics, John Wiley & Sons, Singapore, 1985.

[36] I. Fatt, The network model of porous media, Trans. Am. Inst. Min. Eng. 207 (1956) 144–181.

[37] A. Koponen, M. Kataja, J. Timonen, Permeability and effective porosity of porous media, Phys. Rev. E 56 (3) (1997) 3319–3325.

[38] P. C. Carman, Fluid flow through granular bed, Trans. Inst. Chem. Eng. (London) 15 (1937) 150–156.

[39] G. W. Jackson, D. F. James, The permeability of fibrous porous media, J. Chem. Eng. 64 (1986) 364–374.

[40] J. Happel, Viscous flow relative to arrays of cylinders, AIChE J. 5 (1959) 174–177.

[41] F. A. L. Dullien, Porous Media. Fluid Transport and Pore Structure, Academic Press, San Diego, 1979.

[42] A. Koponen, M. Kataja, J. Timonen, Tortuous flow in porous media, Phys. Rev. E 54 (1) (1996) 406–410.

[43] S. Huang, A. Goel, S. Ramaswamy, B. V. Ramarao, D. Choi, Transverse and in-plane pore structure characterisation of paper, Appita J. 55 (3) (2002) 230–234.

[44] P. M. Adler, Porous media. Geometry and Transports, Butterworth-Heinemann, Boston, 1992.

[45] W. L. Ingmanson, B. D. Andrews, R. C. Johnson, Internal pressure distributions in compressible mats under fluid stress, TAPPI 42 (1959) 840–849.

[46] S. T. Han, Compressibility and permeability of fibre mats, Pulp Paper Mag. Can. 70 (1969) T134–T146.

[47] C. A. León y León, New perspectives in mercury porosimetry, Advances in Colloid and Interface Science 76–77 (1998) 341–372.

[48] S. Kostek, L. M. Schwartz, D. L. Johnson, Fluid permeability in porous media: Comparison of electrical estimates with hydrodynamical calculations, Phys. Rev. B 45 (1) (1992) 186–195.

[49] A. H. Thompson, S. W. Sinton, S. L. Huff, A. J. Katz, R. A. Raschke, G. A. Gist, Deuterium magnetic resonance and permeability in porous media, J. Appl. Phys. 65 (8) (1989) 3259–3263.

[50] D. L. Johnson, D. L. Hemmick, H. Kojima, Probing porous media with first and second sound. I. dynamic permeability, J. Appl. Phys. 76 (1) (1994) 104–114.

[51] G. H. Knauf, M. R. Doshi, Calculations of aerodynamic porosity, specific surface area, and specific volume from Gurley seconds measurements, Tech. Rep. 183, The Institute of Paper Chemistry, Appleton, Wisconsin (1986).

[52] B. Miller, H. Meiser, Uses of the tri liquid/air displacement analyzer, in: Tappi Nonwovens Conference, TAPPI Press, Atlanta, 1989, p. 187.

[53] J. D. Lindsay, The anisotropic permeability of paper, Tappi J. 73 (5) (1990) 223–229.

[54] K. Huang, Statistical mechanics, Wiley, New York, 1967.

[55] H. Chen, S. Chen, W. Matthaeus, Recovery of Navier-Stokes equations using a lattice-gas Boltzmann method, Phys. Rev. A 45 (1992) R5339–R5342.

[56] Y. H. Qian, S. Succi, S. A. Orszag, Recent advances in lattice Boltzmann computing, in: D. Stauffer (Ed.), Annu. Rev. Comp. Phys. III, World Scientific, Singapore, 1996, pp. 195–242.

[57] W. Miller, Flow in the driven cavity calculated by the lattice Boltzmann method, Phys. Rev. E 51 (1995) 3659–3669.

[58] S. Hou, Q. Zou, S. Chen, G. D. Doolen, A. C. Cogley, Simulation of cavity flow by the lattice Boltzmann method, J. Comp. Phys. 118 (1995) 329–347.

[59] P. Skordos, Initial and boundary conditions for the lattice-Boltzmann method, Phys. Rev. E 48 (6) (1993) 4823–4842.

[60] N. S. Martys, J. G. Hagedorn, D. Goujon, J. Devaney, Large scale simulation of single and multicomponent fluid flow in porous media, Proceedings of SPIE 3772 (1999) 205–213.

[61] I. Ginzburg, P. M. Adler, Boundary flow condition analysis for the three-dimensional lattice bolzmann model, J. Phys. II (France) 4 (1994) 191–214.

[62] I. Ginzburg, P. M. Adler, Surface tension models with different viscosities, Transport in porous media 20 (1995) 37–76.

[63] I. Ginzburg, K. Steiner, A free surface lattice-Boltzmann method for modelling the filling of expanding cavities by bingham fluids, Phil. Trans. R. Soc. Lond. A 360 (2002) 453–466.

[64] I. Ginzburg, K. Steiner, Lattice Boltzmann model for free-surface flow and its application to filling process in casting, J. Comp. Phys. 185 (2003) 61–99.

[65] L. Giraud, D. d'Humiéres, P. Lallemand, A lattice Boltzmann model for jeffreys viscoelastic fluid, Europhys. Lett. 42 (1998) 625–630.

[66] M. Bouzidi, D. d'Humiéres, P. Lallemand, L.-S. Luo, Lattice Boltzmann equation on a two-dimensional rectangular grid, J. Comp. Phys. 172 (2001) 704–717.

[67] P. J. Dellar, Incompressible limits of lattice Boltzmann equations using multiple relaxation times, J. Comp. Phys. 190 (2) (2003) 351–370.

[68] M. Gallivan, D. Noble, J. Georgiadis, R. Buckius, An evaluation of the bounce-back boundary condition for lattice-Boltzmann simulations, Int. J. Numer. Meth. Fluids 25 (3) (1997) 249–263.

[69] X. He, Q. Zou, L.-S. Luo, M. Dembo, Some progress in the lattice Boltzmann method. Part i, non-uniform mesh grids, J. Comp. Phys. 129 (1996) 357–363.

[70] R. Cornubert, D. d'Humiéres, D. Levermore, A Knudsen layer theory for lattice gases, Physica D 47 (1–2) (1991) 241–259.

[71] D. Kandhai, A. Koponen, A. Hoekstra, M. Kataja, J. Timonen, P. Sloot, Implementation aspects of 3D lattice-BGK: Boundaries, accuracy and a new fast relaxation method, J. Comp. Phys. 150 (1999) 482–501.

[72] D. Noble, J. Georgiadis, R. Buckius, Direct assessment of lattice Boltzmann hydrodynamics and boundary conditions for recirculating flows, J. Stat. Phys. 81 (1) (1995) 17–33.

[73] D. Noble, S. Chen, J. Georgiadis, R. Buckius, A consistent hydrodynamic boundary condition for the lattice-Boltzmann method, Phys. Fluids 7 (1) (1995) 203–209.

[74] R. Verberg, A. J. C. Ladd, Accuracy and stability of a lattice-Boltzmann model with subgrid scale boundary conditions, Phys. Rev. E 65 (2000) 016701.

[75] Z. Guo, C. Zheng, B. Shi, Discrete lattice effects on the forcing term in the lattice Boltzmann method, Phys. Rev. E 65 (4) (2002) 046308.

[76] X. He, Q. Zou, L.-S. Luo, M. Dembo, Analytic solutions of simple flows and analysis of nonslip boundary conditions for the lattice-Boltzmann-BGK model, J. Stat. Phys. 87 (1–2) (1997) 115–136.

[77] O. Filippova, D. Hänel, Boundary fitting and local grid refinement for lattice-BGK models, Int. J. of Modern Phys. C 9 (8) (1998) 1271–1280.

[78] H. Chen, C. Teixeira, K. Molvig, Realization of fluid boundary conditions via discrete Boltzmann dynamics, Int. J. of Modern Phys. C 9 (8) (1998) 1281–1292.

[79] R. Maier, R. Bernard, D. Grunau, Boundary conditions for the lattice-Boltzmann method, Phys. Fluids 8 (7) (1996) 1788–1801.

[80] S. Chen, D. Martinez, R. Mei, On boundary conditions in lattice-Boltzmann methods, Phys. Fluids 8 (9) (1996) 2527–2536.

[81] I. Ginzbourg, D. d'Humiéres, Local second-order boundary methods for lattice-Boltzmann models, J. Stat. Phys. 84 (5–6) (1996) 927–971.

[82] L. P. Kadanoff, G. R. McNamara, G. Zanetti, From automata to fluid flow: Comparisons of simulation and theory, Phys. Rev. A 40 (8) (1989) 4527–4541.

[83] J. Buick, C. Greated, Gravity in a lattice-Boltzmann model, Phys. Rev. E 61 (5) (2000) 5307–5320.

[84] A. J. C. Ladd, R. Verberg, Lattice-Boltzmann simulations of particle fluid suspensions, J. Stat. Phys. 104 (2001) 1191–1251.

[85] O. Behrend, Solid-fluid boundaries in particle suspension simulations via the lattice Boltzmann method, Phys. Rev. E 52 (1995) 1164–1175.

[86] R. Verberg, A. J. C. Ladd, A lattice-Boltzmann model with sub-grid scale boundary conditions, Phys. Rev. Lett. 84 (2000) 2148–2151.

[87] P. Lallemand, L.-S. Luo, Lattice Boltzmann method for moving boundaries, J. Comp. Phys. 184 (2003) 406–421.

[88] F. Nannelli, S. Succi, Lattice Boltzmann equation on irregular lattices, J. Stat. Phys. 68 (3-4) (1992) 401–407.

[89] A. Koponen, D. Kandhai, E. Hellén, M. Alava, A. Hoekstra, M. Kataja, K. Niskanen, P. Sloot, J. Timonen, Permeability of three-dimensional random fiber webs, Phys. Rev. Lett. 80 (4) (1998) 716–719.

[90] J. Berryman, S. Blair, Use of digital image analysis to estimate fluid permeability of porous media: Application of two-point correlation functions, J. Appl. Phys. 60 (1986) 1930–1938.

[91] R. E. Larson, J. J. L. Higdon, A periodic grain consolidation model of porous media, Phys. Fluids A 1 (1989) 38–46.

[92] A. J. C. Ladd, Hydrodynamic interactions in a suspension of spherical particles, J. Chem. Phys. 88 (1988) 5051–5063.

[93] G. Zanetti, Hydrodynamics of lattice-gas automata, Phys. Rev. A 40 (1989) 1539–1548.

[94] X. He, L.-S. Luo, Lattice Boltzmann model for the incompressible Navier-Stokes equation, J. Stat. Phys. 88 (1997) 927–944.

[95] Z. Lin, H. Fang, R. Tao, Improved lattice-Boltzmann model for incompressible two-dimensional steady flows, Phys. Rev. E 54 (6) (1996) 6323.

[96] T. Pohl, M. Kowarschik, J. Wilke, K. Iglberger, U. Rüde, Optimization and profiling of the cache performance of parallel lattice Boltzmann codes, Parallel Proc. Lett. 13 (4) (2003) 549–560.

[97] C. Pan, J. F. Prins, C. T. Miller, A high-performance lattice Boltzmann implementation of multiphase flow in porous media, Comp. Phys. Comm. 158 (2) (2004) 89–105.

[98] Z. Guo, T. S. Zhao, Y. Shi, Preconditioned lattice-Boltzmann method for steady flows, Phys. Rev. E 70 (4) (2004) 066706.

[99] A. F. Bennett, J. R. Taylor, B. S. Chua, Lattice Boltzmann open boundaries for hydrodynamic models, J. Comp. Phys. 203 (1) (2005) 89–111.

[100] W. E. Langlois, Slow Viscous Flow, Macmillan, New York, 1964.

[101] J. A. Åström, J. P. Mäkinen, J. Timonen, Modeling multilayer woven fabrics, Appl. Phys. Lett. 79 (2) (2001) 180–181.

[102] K. J. Niskanen, M. J. Alava, Planar random networks with flexible fibers, Phys. Rev. Lett. 73 (25) (1994) 3475–3478.

[103] B. Biswal, C. Manwart, R. Hilfer, S. Bakke, P. Oren, Quantitative analysis of experimental and synthetic microstructures for sedimentary rock, Physica A 273 (1999) 452–475.

[104] S. Bakke, P. Oren, 3-D pore-scale modeling of sandstones and flow simulations in pore networks, SPE J. 2 (1997) 136–149.

[105] M. Sahimi, D. Stauffer, Efficient simulation of flow and transport in porous media, Chem. Eng. Sci. 9 (1991) 2225–2233.

[106] C. Manwart, S. Torquato, R. Hilfer, Stochastic reconstruction of sandstones, Phys. Rev. E 62 (2000) 893.

[107] K. J. Niskanen, M. J. Alava, E. Hellén, M. Alava, KCL-PAKKA: Simulation of the 3D structure of paper, in: The Fundamentals of Papermaking Materials, The Eleventh Fundamental Research Symposium, Pira International, 1997, pp. 1177–1213.

[108] D. Qi, T. Uesaka, Numerical experiments on paper-fluid interaction - permeability of 3-D anisotropic fibre network, J. Mat. Sci. 31 (18) (1996) 4865–4870.

[109] E. J. Samuelsen, Ø. W. Gregersen, P. J. Houen, T. Helle, C. Raven, A. Snigirev, Three-dimensional imaging of paper by use of synchrotron X-ray microtomography, J. Pulp Pap. Sci. 27 (2) (2001) 50–53.

[110] E. J. Samuelsen, T. Helle, P. J. Houen, Ø. W. Gregersen, C. Raven, Three-dimensional imaging of paper by use of synchrotron X-ray microtomography, in: TAPPI International Paper Physics conference, TAPPI Press, Atlanta, 1999, pp. 307–312.

[111] T. E. Gureyev, R. Evans, A. W. Stevenson, D. Gao, S. W. Wilkins, X-ray phase-contrast microscopy of paper, TAPPI J. 84 (2) (2001) 52.

[112] A. Goel, M. Tzanakakis, S. Huang, S. Ramaswamy, D. Choi, B. V. Ramarao, Characterization of the three-dimensional structure of paper using X-ray microtomography, TAPPI J. 84 (5) (2001) 1–8.

[113] C. Antoine, P. Nygård, Ø. W. Gregersen, T. Weitkamp, C. Rau, 3D images of paper obtained by phase-contrast X-ray microtomography: image quality and binarisation, Nucl. Inst. Meth. Phys. Res. A 490 (2002) 392–410.

[114] S. R. Sternberg, Biomedical image processing, IEEE Comp. 16 (1) (1983) 22–34.

[115] M. Aronsson, On 3D fibre measurements of digitized paper, Ph.D. thesis, Swedish University of Agricultural Sciences (2002).

[116] D. Choi, S. Ramaswamy, In-plane permeability characteristics in paper board, AIChE Symposium Series 96 (324) (2000) 80.

[117] J. D. Lindsay, P. H. Prady, Studies of anisotropic permeability with applications to water removal in fibrous webs, Tappi J. 76 (9) (1993) 119–127.

[118] D. Zhang, R. Zhang, S. Chen, W. E. Soll, Pore scale study of flow in porous media: Scale dependency, REV, and statistical REV, Geophys. Res. Lett. 27 (8) (2000) 1195–1198.

[119] T. Bourbie, B. Zinszner, Hydraulic and acoustic properties as a function of porosity in Fontainebleau sandstone, J. Geophys. Res. 90 (B13) (1985) 11524–11532.

[120] T. Bourbie, O. Coussy, B. Zinszner, Acoustics of porous media, Editions Technip, Paris, 1987.